

Search for Sterile Neutrinos at the Short Baseline Neutrino Program

Thomas Ham
Univeristy of Liverpool

Some more stuff

Acknowledgements

Acknowledgements . . .

Abstract

Abstract..

Declaration

Declaration

Name??

Contents

Glossary	vii
1. Neutrino Physics	1
1.1. A Brief History of Neutrino Discoveries	1
1.2. Overview of Neutrino Physics	3
1.2.1. Helicity and Chirality	4
1.2.2. Weak Interactions and CP violation	5
1.2.3. Neutrino Oscillations	7
1.3. Motivation for Sterile Neutrinos	12
1.3.1. LSND	13
1.3.2. MiniBooNE	14
1.3.3. Gallium Anomaly	16
1.3.4. Reactor Anomaly	16
1.3.5. Theoretical Motivation	16
1.4. Theory of Sterile Neutrinos	17
1.4.1. Neutrino Mass	17
1.4.2. Sterile Neutrino Oscillations	20
2. The Short Baseline Neutrino Program	22
2.1. SBN Program Overview	22
2.2. Liquid Argon Time Projection Chambers	23
2.2.1. LArTPC Design	24
2.2.2. Detector effects	25
2.3. Booster Neutrino Beam	29
2.4. Neutrino Interactions	32
2.5. SBND	37

2.6. MicroBooNE	41
2.7. ICARUS	44
2.8. SBN Physics Capabilities	45
3. Sterile Neutrino Oscillation Inputs Within SBN	50
3.1. Event Production	50
3.2. Event Selection	52
3.2.1. ν_μ Selection	53
3.2.2. ν_e Selection	53
3.3. Reaction Modes	55
3.4. Systematic Uncertainties	58
3.4.1. Flux Systematics	58
3.4.2. Interaction Systematics	62
3.4.3. Other Systematics	69
3.5. Other Analysis Choices	72
3.5.1. Baseline	72
3.5.2. Binning	76
A. Pointless extras	78
B. Single Parameter Variations	79
Bibliography	83

Glossary

ADC Analog Digital Converter.

APA Andode Plane Assembly.

ARAPUCA Argon R&D Advanced Program at UniCAMP.

ArgoNeuT Argon Neutrino Test Stand.

BNB Booster Neutrino Beam.

BSM Beyond Standard Model.

CC Charged Current.

CCQE Charged Current Quasi Elastic.

CP charge-parity.

CPA Cathode Plane Assembly.

CRT Cosmic Ray Tagger.

DIS Deep Inelastic Scattering.

DONUT Direct Observation of the Nu Tau.

DUNE Deep Underground Neutrino Experiment.

EM electromagnetic.

ES Elastic Scattering.

Fermilab Fermi National Accelerator Laboratory.

GALLEX Gallium Experiment.

GEANT4 GEometry ANd Tracking.

GENIE Generates Events for Neutrino Interaction Experiments.

ICARUS Imaging Cosmic and Rare Underground Signals.

KARMEN Karlsruhe Rutherford Medium Energy Neutrino.

LAr Liquid Argon.

LArSoft Liquid Argon Software.

LArTPC Liquid Argon Time Projection Chamber.

LEP Large Electron-Positron Collider.

LSND Liquid Scintillator Neutrino Detector.

MC Monte Carlo.

MCT Monte Carlo Template.

MEC Meson Exchange Current.

MicroBooNE Micro Booster Neutrino Experiment.

MiniBooNE Mini Booster Neutrino Experiment.

MINOS Main Injector Neutrino Oscillation Search.

MIP Minimum Ionising Particle.

NC Neutral Current.

NIST National Institute of Standards and Technology.

P parity.

PDG Particle Data Group.

PDS Photon Detection System.

PMNS Pontecorvo-Maki-Nakagawa-Sakata.

PMT Photo Multiplier Tube.

POT Protons-On-Target.

SAGE Soviet-American Gallium Experiment.

SBN Short Baseline Neutrino.

SBND Short Baseline Near Detector.

SCE Space Charge Effect.

SciBooNE SciBar Booster Neutrino Experiment.

SiPM Silicon Photomultiplier.

SK Super Kamiokande.

SM Standard Model.

SNO Sudbury Neutrino Observatory.

SP Space Point.

T2K Tokai to Kamioka.

TPB Tetraphenyl Butadiene.

TPC Time Projection Chamber.

VALOR VALEncia-Oxford-Rutherford.

VUV Vacuum Ultra Violet.

List of figures

1.1.	Elementary particle classifications.	3
1.2.	Neutrino hierarchy.	12
1.3.	LSND excess.	14
1.4.	MiniBooNE excess.	15
2.1.	SBN map.	22
2.2.	Schematic of LArTPC detector.	25
2.3.	Schematic of the BNB layout.	30
2.4.	Neutrino fluxes in SBN.	31
2.5.	Feynman diagrams of possible Meson Exchange Current (MEC) interactions.	34
2.6.	Feynman diagrams of the Charged Current (CC) processes most commonly expected in Short Baseline Neutrino (SBN).	36
2.7.	Feynman diagrams of the Neutral Current (NC) processes most commonly expected in SBN.	37
2.8.	Schematic of the SBN detector.	38
2.9.	CRT positioning in SBND.	39
2.10.	ARAPUCA operating principle.	41
2.11.	Schematic of PDS box.	42
2.12.	MicroBooNE detector.	43
2.13.	ICARUS detector.	45
2.14.	SBN oscillation probability.	47
2.15.	ν_e appearance SBN proposal sensitivity.	48
3.1.	SBN Oscillation analysis paradigm.	51
3.2.	Example efficiency uncertainty covariance matrices.	71

3.3.	Possible event migration due to uncertainty on the reconstructed neutrino energy	72
3.4.	The baseline distribution of events in the ν_μ sample for each of the SBN detectors	74
3.5.	ν_e baseline distributions	74
3.6.	Oscillation probability for different baseline parametrisations	75
B.1.	Flux systematic parameter validation	79
B.2.	Proposal interaction systematic parameter validation	80
B.3.	Modern interaction systematic parameter validation	81

List of tables

1.1.	3-flavour neutrino best fit values.	13
1.2.	Best fit value for sterile oscillation parameters.	21
2.1.	Hadron decay mode in the BNB.	30
2.2.	BNB flavour composition.	31
3.1.	Events generated as part of the ν_e sample.	52
3.2.	Fine Reaction Modes.	56
3.3.	Coarse Reaction Modes.	57
3.4.	Optical, beam focusing flux systematic parameters.	59
3.5.	Hadronic secondary interaction flux systematic parameters.	60
3.6.	Hadronic neutrino production flux systematic parameters.	61
3.7.	SBN proposal interaction cross-section systematic parameters.	66
3.8.	Modern interaction cross-section systematic parameters.	67
3.9.	Intranuclear hadron transport systematic parameters.	68
3.10.	Binning scheme for the efficiency uncertainties.	70

Chapter 1.

Neutrino Physics

1.1. A Brief History of Neutrino Discoveries

The neutrino was first postulated in 1930 by Pauli in an attempt to explain the continuous energy spectrum observed for the electrons from beta decay experiments [1]. At the time it was assumed that along with the nucleus, an electron was the only other product from beta decays. That is, beta decay was thought to be a two body decay of the following form,

$${}^A_Z X \longrightarrow {}^A_{Z+1} Y + e^-, \quad (1.1)$$

where X and Y are the element undergoing the decay and the resultant element respectively. The continuous energy spectrum of the electron was puzzling as it was expected that the electron would always have a fixed kinetic energy and observing electrons with a range of energies appeared to violate energy conservation. Pauli theorised that in addition to the electron, a neutral particle was also emitted in beta decays and that the sum of the energy of the electron and this neutral particle would be constant [1].

The (electron) neutrino wasn't experimentally confirmed until 1956 by Cowan and Reines who used a nuclear reactor as their neutrino source [2]. Their detector consisted of two tanks of water in which cadmium chloride had been dissolved, interlaced between three tanks of liquid scintillator. When the electron anti-neutrinos would interact with

protons in one of the water tanks via inverse beta decay, a neutron and positron would be produced. The positron would then quickly annihilate with an electron producing two gamma rays. The cadmium would absorb the neutron and then emit a single gamma ray. The liquid scintillator was surrounded by Photo Multiplier Tubes (PMTs) and the signal for the experiment was two gamma rays from the electron-positron annihilation shortly followed by another gamma ray from the absorption of the neutron [2].

The second type of neutrino to be discovered was the muon neutrino by the Alternating Gradient Synchrotron at Brookhaven National Laboratory in 1962. The neutrinos were predominantly produced from charged pion decays which in turn were produced by firing a beam of protons at a beryllium target. The pions were directed in the direction of an iron wall during which they have the chance to decay. The iron wall was designed to absorb muons and other interacting particles. The neutrinos were then detected by an aluminium spark chamber located behind the shield [3].

Following the discovery of the tau lepton in 1975 by the SLAC National Accelerator Laboratory, the tau neutrino was predicted in order to mirror the structure of the electron and muon lepton both of which have an associated neutrino [4]. The existence of the tau neutrino was eventually confirmed by the Direct Observation of the Nu Tau (DONUT) experiment in 2000. The DONUT experiment used a neutrino beam created from the decay of charmed mesons produced by protons from the Tevatron accelerator at Fermi National Accelerator Laboratory (Fermilab). Most of the tau neutrinos were produced from the decay of the D_s meson and the decay from the resulting tau lepton [5].

More detail on the experiments?

The three confirmed flavours of neutrinos (ν_e, ν_μ, ν_τ) are consistent with predictions from the Standard Model (SM). The number of expected neutrinos may be determined from the decay of the Z-boson since it's lifetime is dependent on the number of flavours. This was shown by the Large Electron-Positron Collider (LEP) experiment, which found the lifetime of the Z-boson to be consistent with a three neutrino model [6] [7]. There have, however, been results from experiments which are inconsistent with the 3 neutrino framework. Namely the excess of events observed by the Liquid Scintillator Neutrino Detector (LSND) and Mini Booster Neutrino Experiment (MiniBooNE) experiments, the deficit of events observed by the Soviet-American Gallium Experiment (SAGE) and Gallium

Experiment (GALLEX) detectors (dubbed the *Gallium Anomaly*) and the deficit of events observed from nuclear reactors (dubbed the *Reactor Anomaly*) [8] [9] [10] [11] [12] [13]. Additional neutrino flavours may exist and not contradict the statement on the lifetime of the Z-boson if they have a mass greater than half that of the Z-boson and/or they do not weakly interact and hence don't contribute to the decay rate of the Z-boson [6]. The hypothetical neutrinos which do not weakly interact are known as *sterile* neutrinos in order to distinguish them from the *active* ones that do. Sterile neutrinos will be discussed in greater detail in Section 1.3 and Section 1.4.

1.2. Overview of Neutrino Physics

Elementary particles are classified as either fermions or bosons which are typically considered *matter particles* and *force carrier particles* respectively. The particles are classified on whether they follow either Fermi-Dirac or Bose-Einstein statistics. Fermions are then sub-divided between leptons and quarks, with one of the defining differences being that quarks experience the strong force along with the other three fundamental forces whereas the leptons only experience gravity, the weak and the electromagnetic forces. The bosons are subdivided into gauge and scalar bosons depending on the spin of the particle. Gauge bosons have a spin of 1 whereas scalar bosons have a spin of 0 [14]. The classification of elementary particles is shown in the flow chart in Figure 1.1.

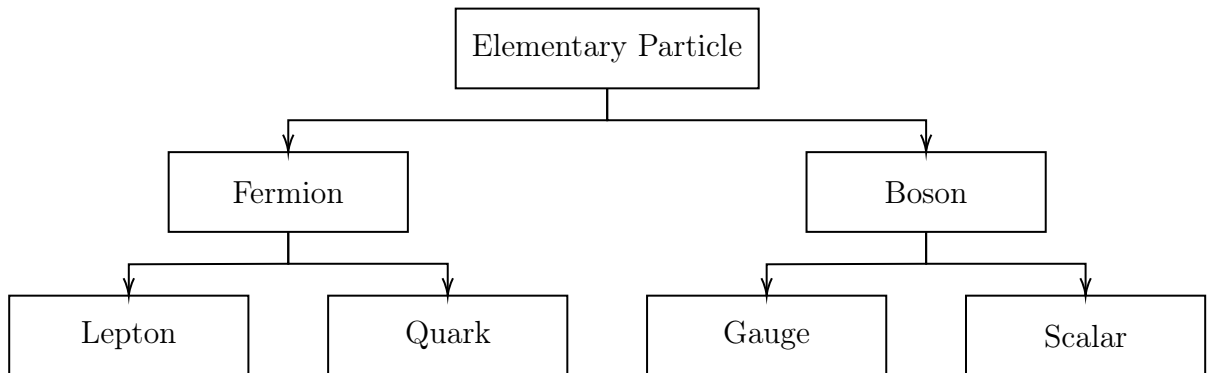
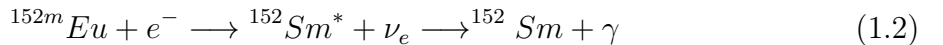


Figure 1.1.: Elementary particle classifications.

Since neutrinos are neutral fermions, it is possible that neutrinos are their own anti-particle (a Majorana Particle). This idea was first proposed in 1937 by Majorana [15]. Within the SM, all fermions with the possible exception of neutrinos behave as Dirac fermions, that is, the particle and anti-particle are distinct [16]. With the possibility that neutrinos are Majorana in nature, it has led to the search for neutrinoless double beta decay [17]. This is a variation on ordinary double beta decay in which a nucleus decays by emitting two electrons simultaneously. In ordinary double beta decay there would also be two (anti)neutrinos in the final state, however, if neutrinos are Majorana particles, it can be thought of as one nucleon emitting a neutrino and the other absorbing it hence there are no neutrinos in the final state. Observation of such a decay would confirm the Majorana nature of neutrinos and give direct evidence for physics beyond the SM since the lepton number would not be conserved. Furthermore, neutrino oscillations (which is discussed in Section 1.2.3) are at odds with the SM assumption that neutrinos are massless. With the requirement that neutrinos are indeed massive, the Dirac or Majorana nature of neutrinos is again discussed in Section 1.4.1 within the context of mass generation mechanisms [18].

1.2.1. Helicity and Chirality

The helicity of a particle is defined as the projection of its spin onto the linear momentum. If the spin is aligned with the direction of motion, the particle is said to be *right-handed* and has an eigenvalue equal to +1 whereas if the spin is aligned in the opposite direction a particle is said to be *left-handed* and has an eigenvalue equal to -1 [19]. It was observed by Goldhaber and others that neutrinos appear to exclusively have left-handed helicities (and right-handed helicities for anti-neutrinos). The experiment they used to determine this was as follows; consider the decay of an isomer of europium via electron capture to an excited state of samarium. The samarium nucleus then decays to its ground state by emitting a photon.



To conserve momentum, the excited samarium nucleus must recoil in a direction opposite to the emitted neutrino. To conserve angular momentum the spin of the neutrino and the recoiling nucleus must be in opposite directions which means that they both have the

same handedness. Finally, the photon emitted will have a spin in the opposite direction to the neutrino and if the photon is emitted in a direction opposite to the neutrino direction, both will have the same helicity. The photons emitted in the direction opposite to the neutrino were identified, their helicity determined and it was found that they were all left-handed [20].

Helicity does commute with the Hamiltonian, however it is not Lorentz invariant (for massive particles) [21]. Since massive particles travel at speeds less than c , it is always possible to boost to a frame such that the direction of motion is reversed. Spin is not affected by this which means that it is possible for the sign of the helicity to change. In contrast to helicity, chirality is a Lorentz invariant quantity that does not commute with the Hamiltonian. The chirality operator is γ^5 and it is defined as $i\gamma^0\gamma^1\gamma^2\gamma^3$ (i.e. i times the product of the gamma matrices). Similarly to helicity, when the chirality operator acts on the eigenfunctions ψ_R and ψ_L it results in an eigenvalue of +1 and -1 respectively. It is commonly expressed in term of projection operators $P_{(L,R)}$ such that,

$$\begin{aligned}\psi_L &= P_L \psi \equiv \frac{1 - \gamma^5}{2} \psi \\ \psi_R &= P_R \psi \equiv \frac{1 + \gamma^5}{2} \psi,\end{aligned}\tag{1.3}$$

where ψ is a spinor which can be written in terms of left and right chiral components, $\psi = \psi_L + \psi_R$. Since $P_{(L,R)}^\dagger = P_{(L,R)}$ and $P_{(L,R)}\gamma^0 = \gamma^0 P_{(R,L)}$, it follows that

$$\overline{\psi}_L \psi_L = \overline{\psi}_R \psi_R = 0.\tag{1.4}$$

It should be noted that for massless particles, helicity is Lorentz invariant and becomes identical to chirality. [22]

1.2.2. Weak Interactions and CP violation

NOT SURE I LIKE HOW THIS SECTION FLOWS..

The weak force is mediated by the charged W^\pm and neutral Z^0 bosons and is responsible for radioactive decay. It is dubbed *weak* because if the strong or electromagnetic (EM)

forces are also present the weak force is usually subdominant. The active neutrinos only interact via the weak force (and gravity) which is one of the reasons they have been historically difficult to detect.

It was shown experimentally by Wu that parity (P) conservation is violated and later by Cronin and Fitch that charge-parity (CP) conservation is also violated [23] [24]. CP violation is one of the Sakharov conditions required to have a matter-antimatter asymmetry in the universe, however, the amount of CP violation seen in the quark sector is seemingly insufficient to explain the matter dominated universe we observe [25]. There may also be CP violation from the Pontecorvo-Maki-Nakagawa-Sakata (PMNS) matrix in the lepton sector which could help explain the matter-antimatter asymmetry. However, the amount of CP violation in the lepton sector, if any, is currently unknown [26].

The weak charged current, j_{weak}^{CC} may be expressed as,

$$j_{weak}^{CC} = \frac{g_w}{\sqrt{2}} \bar{\psi} \gamma^\mu \frac{1}{2} (1 - \gamma^5) \psi, \quad (1.5)$$

where g_w is the coupling factor [14]. This has the form of a vector-axial (V-A) interaction, where the vector current is given by $\bar{\psi} \gamma^\mu \psi$ and the axial current is given by $\bar{\psi} \gamma^\mu \gamma^5 \psi$. The axial component remains unchanged under a parity transformation, whereas the sign of the vector component changes. We are usually interested in the square of the amplitude, which in short means taking the square of the weak current. This results in a squared vector and axial component plus a cross term. Since the axial and vector components behave differently under a parity transformation, this cross term leads to parity violation [22].

Because the projection operator, P_L , appears in Equation 1.5 it follows that weak interactions only apply to left-handed particles (and right-handed antiparticles). Neutrinos only interact via the weak force which means they are therefore produced with a left-handed chirality and since they are ultra-relativistic, for all intents and purposes they also have a left-handed helicity [27].

1.2.3. Neutrino Oscillations

Another unique property of neutrinos are their ability to oscillate. That is, the neutrino flavour may change as it propagates. This phenomenon was first proposed by Pontecorvo in 1957 [28]. In the following years this work was built upon by Maki, Nakagawa, Sakata and Pontecorvo himself [29].

One of the first experimental results to eventually be explained by neutrino oscillations was the Homestake experiment. This was an experiment in the 1960's that was designed to count the number of solar neutrinos. The crux of the experiment was to fill an underground tank with dry-cleaning fluid (perchloroethylene) since it contains chlorine. The solar neutrinos would be detected by inverse beta decay via



where the argon would be extracted and counted as it decayed. From this, the number of interacting electron neutrinos was determined, however this number was consistently about a third of the number expected by solar predictions. This inconsistency was later dubbed the *Solar Neutrino Problem* [30].

The ratio of muon to electron neutrinos produced in the atmosphere from the decay of pions and muons was also studied. The predicted rate of neutrinos in the atmosphere was thought to be well understood, however a number of experiments, the most notable of which, Super Kamiokande (SK), all observed ratios significantly below the expected value. This indicated a deficit in the observed muon neutrinos or an excess in electron neutrinos (or both). Mirroring the solar neutrino problem, these observations were dubbed the *Atmospheric Neutrino Anomaly* [31].

In addition to measuring the ratio of atmospheric neutrinos, SK was also able to measure the zenith angle of the incoming neutrinos. This allowed the observed and predicted number of neutrinos to be compared as a function of the zenith angle. It was noted that the number of electron neutrinos agreed reasonably well with the expected value across all angles whereas for low energy muon neutrinos there was a deficit of events for all angles and for high energy muons there was a deficit of events for zenith angles corresponding to large distances travelled (e.g. neutrinos which travelled through the earth

and into the detector from below). The observed rate of high energy muons at angles corresponding to travelling directly down from the atmosphere to the detector agreed with predicted values [32].

The results published by SK in 1998 allowed the atmospheric neutrino anomaly to be reconciled with neutrino oscillations and was the first time neutrino oscillations were confirmed to have been observed [32]. Shortly after, in 2001, the Sudbury Neutrino Observatory (SNO) resolved the solar neutrino problem by again explaining the deficit in observed electron neutrinos as a result of neutrino oscillations. The SNO detector was designed with the intention of being able to measure the total neutrino flux (the sum of all three flavours) and the electron neutrino flux in isolation. The detector consisted of a tank of heavy water. Solar neutrinos have sufficient energy to interact via NC interactions with the deuterium in the heavy water regardless of neutrino flavour,

$$\nu + d \longrightarrow \nu + p + n. \quad (1.7)$$

Neutrinos of any flavour may also interact via Elastic Scattering (ES),

$$\nu + e^- \longrightarrow \nu + e^-, \quad (1.8)$$

but the sensitivity to ν_μ and ν_τ are reduced. Finally, only electron neutrinos may interact via CC,

$$\nu_e + d \longrightarrow p + p + e^-, \quad (1.9)$$

therefore this channel only measured the flux of ν_e . Confirmation that the flux of ν_e was less than the flux from the NC or ES channels coupled with the fact that the ν_e flux was in agreement with previous solar neutrino experiments was sufficient to resolve the solar neutrino problem [33].

Neutrino oscillations is one of the key topics in the field and this thesis. In the remainder of this section we will discuss the theory of neutrino oscillations. The three flavour states $(\nu_e, \nu_\mu, \nu_\tau)$ have already been established, but with the confirmation of neutrino oscillations, the three corresponding mass states (ν_1, ν_2, ν_3) are required to be distinct from the flavour states. The flavour eigenstate of a neutrino is what is observed, however each flavour state

is a superposition of the three mass states. As a neutrino propagates, the mass states propagate at different rates and thus the relative phase between the states is continuously changing. When a neutrino then interacts, it will have a certain set of mass states which correspond to a superposition of the flavour states. The flavour superposition will then collapse into a single flavour and this is what is then detected. This is the mechanism which allows neutrino flavours to oscillate.

The transformation between the flavour and mass states may be expressed as

$$|\nu_\alpha\rangle = \sum_k U_{\alpha k}^* |\nu_k\rangle, \quad (1.10)$$

where $\alpha \in (e, \mu, \tau)$, $k \in (1, 2, 3)$ and U is a unitary rotation matrix. In the case of three flavour neutrino oscillations, U , is known as the PMNS mixing matrix which is a 3×3 matrix representing the three different states [22]. The PMNS matrix is parameterised in terms of three mixing angles ($\theta_{12}, \theta_{13}, \theta_{23}$) and a CP violating phase, δ_{cp} , as

$$\begin{aligned} U &= \begin{pmatrix} U_{e1} & U_{e2} & U_{e3} \\ U_{\mu 1} & U_{\mu 2} & U_{\mu 3} \\ U_{\tau 1} & U_{\tau 2} & U_{\tau 3} \end{pmatrix} \\ &= \begin{pmatrix} 1 & 0 & 0 \\ 0 & c_{23} & s_{23} \\ 0 & -s_{23} & c_{23} \end{pmatrix} \begin{pmatrix} c_{13} & 0 & s_{13} e^{-i\delta_{cp}} \\ 0 & 1 & 0 \\ -s_{13} e^{i\delta_{cp}} & 0 & c_{13} \end{pmatrix} \begin{pmatrix} c_{12} & s_{12} & 0 \\ -s_{12} & c_{12} & 0 \\ 0 & 0 & 1 \end{pmatrix} \end{aligned} \quad (1.11)$$

where $c_{kj} = \cos \theta_{kj}$ and $s_{kj} = \sin \theta_{kj}$.

Since the neutrino mass states are eigenstates of the Hamiltonian, H , the time evolution of the mass states is given by the time dependent Schrödinger equation

$$i \frac{d}{dt} |\nu_k(t)\rangle = H |\nu_k(t)\rangle. \quad (1.12)$$

It can be seen that the solution to Equation 1.12 is given by a plane wave solution

$$|\nu_k(t)\rangle = e^{-iE_k t} |\nu_k\rangle. \quad (1.13)$$

The amplitude of a transition, $A_{\nu_\alpha \rightarrow \nu_\beta}(t)$, is defined as the projection of the final state onto the initial state, so for flavour oscillations the amplitude is given by

$$A_{\nu_\alpha \rightarrow \nu_\beta}(t) \equiv \langle \nu_\beta | \nu_\alpha(t) \rangle. \quad (1.14)$$

The probability of transition, $P_{\nu_\alpha \rightarrow \nu_\beta}(t)$, is then given by the absolute square of the amplitude

$$P_{\nu_\alpha \rightarrow \nu_\beta}(t) = |A_{\nu_\alpha \rightarrow \nu_\beta}(t)|^2. \quad (1.15)$$

It follows from Equation 1.10 and Equation 1.13 that

$$|\nu_\alpha(t)\rangle = \sum_k U_{\alpha k}^* e^{-iE_k t} |\nu_k\rangle \quad (1.16)$$

and that the transition amplitude is given by

$$A_{\nu_\alpha \rightarrow \nu_\beta}(t) = \sum_k U_{\alpha k}^* U_{\beta k} e^{-iE_k t} \quad (1.17)$$

where we have used the fact that $\langle \nu_j | \nu_k \rangle = \delta_{jk}$ since the mass eigenstates are orthonormal. It then follows that the oscillation probability is given by

$$P_{\nu_\alpha \rightarrow \nu_\beta}(t) = \sum_{k,j} U_{\alpha k}^* U_{\beta k} U_{\alpha j} U_{\beta j}^* e^{-i(E_k - E_j)t}. \quad (1.18)$$

Under the assumption that neutrinos are relativistic, the mass state energy, E_k , may be expressed in terms of the neutrino energy, E ,

$$E_k = \sqrt{|\vec{p}|^2 + m_k^2} \simeq E + \frac{m_k^2}{2E}. \quad (1.19)$$

By noting that the mass splitting, Δm_{kj}^2 , is defined as

$$\Delta m_{kj}^2 = m_k^2 - m_j^2 \quad (1.20)$$

and that for highly relativistic particles $t \approx L$, where L is known as the baseline (i.e. the distance the neutrino has travelled), the oscillation probability may be written as

$$P_{\nu_\alpha \rightarrow \nu_\beta}(L, E) = \sum_{k,j} U_{\alpha k}^* U_{\beta k} U_{\alpha j} U_{\beta j}^* e^{-i \frac{\Delta m_{kj}^2 L}{2E}}. \quad (1.21)$$

Finally, in a two flavour oscillation regime, the oscillation probability may be simplified to

$$P_{\nu_\alpha \rightarrow \nu_\beta} = \begin{cases} \sin^2(2\theta) \sin^2(\frac{\Delta m^2 L}{4E}), & \nu_\alpha \neq \nu_\beta \\ 1 - \sin^2(2\theta) \sin^2(\frac{\Delta m^2 L}{4E}), & \nu_\alpha = \nu_\beta, \end{cases} \quad (1.22)$$

where the mixing matrix has been reduced to a rotation matrix [22].

It should be noted that what neutrino experiments probe is the mass splitting and not the absolute neutrino masses. It is understood from oscillation experiments that Δm_{21}^2 , known as the solar mass splitting, is equal to 7.5×10^{-5} eV² and that $|\Delta m_{31}^2|$, known as the atmospheric mass splitting, is equal to 2.4×10^{-3} eV². The sign of the atmospheric mass splitting is however unknown i.e. it is an open question whether m_3 is the heaviest or the lightest neutrino mass state. This leads to two possibilities, the so called *normal hierarchy* where the neutrino mass states increase from $m_{1 \rightarrow 2 \rightarrow 3}$ or the *inverted hierarchy* where the mass states increase from $m_{3 \rightarrow 1 \rightarrow 2}$. The best fit values for oscillation parameters and the CP violating phase from a 3-flavour neutrino framework are shown in Table 1.1 for both the normal and inverted hierarchy. The numbers have been provided by the 2020 edition of the Particle Data Group (PDG) collaboration [34].

The nature of the neutrino hierarchy has major impacts on several areas. Within the inverted hierarchy, there is a lower bound on the Majorana mass of the electron neutrino mass. If neutrinoless double beta decay experiments can put bounds on the neutrino mass below this, the inverted hierarchy may be ruled out (under the assumption that neutrinos are Majorana in nature). Alternatively, if the inverted hierarchy is realised, neutrinoless double beta experiments are promising ways to determine whether neutrinos are Majorana particles or not. There are also a number of theories which predict either the normal or inverted hierarchy, so determining the hierarchy will be a strong motivator in determining the credibility of a given theory [35].

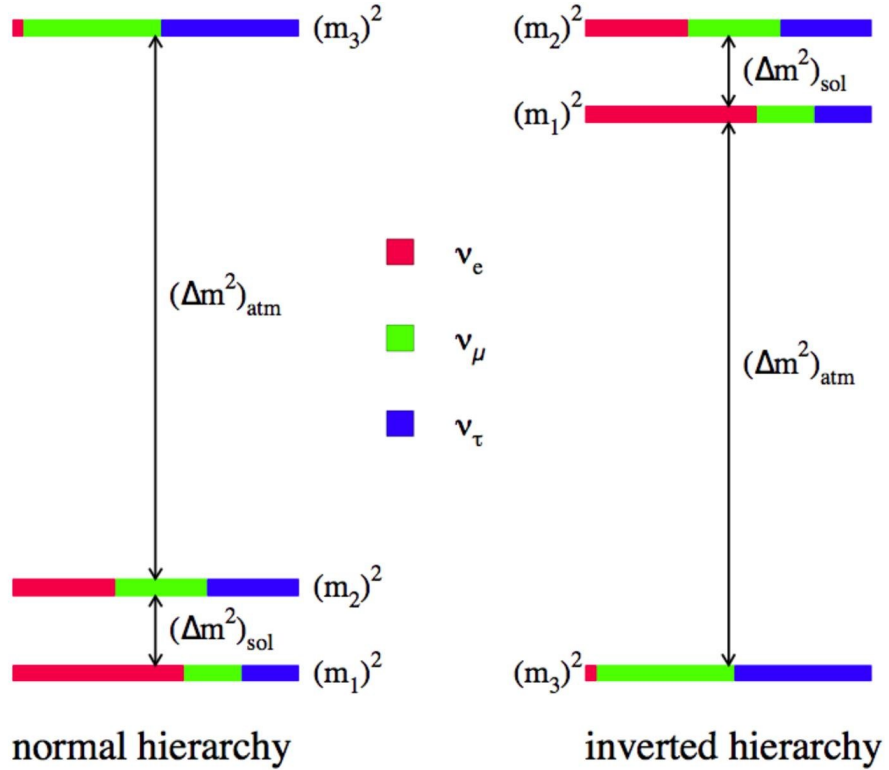


Figure 1.2.: Diagrammatic representation of the normal hierarchy (left) and the inverted hierarchy (right). The flavour contributions to each mass state are illustrated by the different colours [36].

1.3. Motivation for Sterile Neutrinos

There have been a number of experimental results which are not consistent with oscillations in a three neutrino model. Most of these anomalous results can be explained by oscillations with one or more eV scale neutrinos pointing towards the existence of at least one light sterile neutrino. The experiments which have seen results seemingly in favour of eV scale sterile neutrinos will be discussed in the upcoming sections. There are however tensions between the results in favour of additional neutrino flavours and the null results from experiments such as Karlsruhe Rutherford Medium Energy Neutrino (KARMEN) and Main Injector Neutrino Oscillation Search (MINOS) [37]. The KARMEN experiment was sensitive to $\nu_\mu \rightarrow \nu_e$ and $\bar{\nu}_\mu \rightarrow \bar{\nu}_e$ over a baseline of 17.6 m. No evidence of oscillations were found and a 90% confidence level exclusion limit was placed on $\Delta m^2 > 100 \text{ eV}^2$ with $\sin^2 2\theta < 4 \times 10^{-2}$

Parameter	Best Fit	
	Normal Hierarchy	Inverted Hierarchy
$\sin^2 2\theta_{12}$	0.307 ± 0.013	0.307 ± 0.013
$\sin^2 2\theta_{13}$	$(2.20 \pm 0.07) \times 10^{-2}$	$(2.20 \pm 0.07) \times 10^{-2}$
$\sin^2 2\theta_{23}$	0.546 ± 0.021	0.539 ± 0.022
Δm_{21}^2	$(7.53 \pm 0.18) \times 10^{-5} \text{ eV}^2$	$(7.53 \pm 0.18) \times 10^{-5} \text{ eV}^2$
Δm_{32}^2	$(2.453 \pm 0.033) \times 10^{-3} \text{ eV}^2$	$(-2.536 \pm 0.034) \times 10^{-3} \text{ eV}^2$
δ_{CP}	$1.36^{+0.20}_{-0.16} \pi \text{ rad}$	$1.36^{+0.20}_{-0.16} \pi \text{ rad}$

Table 1.1.: The best fit values for 3-flavour neutrino oscillation parameters from the 2020 PDG [34].

and $\sin^2 2\theta < 8.5 \times 10^{-3}$ for neutrinos and anti-neutrinos respectively [38]. The MINOS experiment used a predominantly muon-neutrino beam with a peak energy of 3 GeV with the near detector being at a baseline of 1.04 km. Again, no evidence of oscillations was observed. For a mass splitting of $\Delta m_{42}^2 = 0.5 \text{ eV}^2$, the value of $\sin^2 2\theta_{24}$ was constrained to be less than 0.016 for a 90% confidence level [39].

1.3.1. LSND

The LSND experiment involved a close to 800 MeV proton beam which produced mainly π^+ and was designed to focus on the search for $\bar{\nu}_\mu \rightarrow \bar{\nu}_e$ appearance where the $\bar{\nu}_\mu$'s were a result from the decay of anti-muons which in turn were produced from the decay of at rest π^+ . The detector consisted of a tank filled with 167 tons of liquid scintillator positioned 30 m from the neutrino beam source and was able to detect both Cerenkov and scintillation light. The $\bar{\nu}_e$ appearance signal was identified from the $\bar{\nu}_e + p \rightarrow e^+ + n$ reaction with the signature of the reaction being the energy of the e^+ and the energy of a gamma as a result of neutron capture on a free proton. The LSND experiment observed an excess of $87.96 \pm 22.46 \pm 6.0$ events from $\bar{\nu}_e + p \rightarrow e^+ + n$ reactions which corresponds to a 3.8σ excess which is shown in Figure 1.3 [8]. This was the first experiment to point towards the existence of an eV scale neutrino.

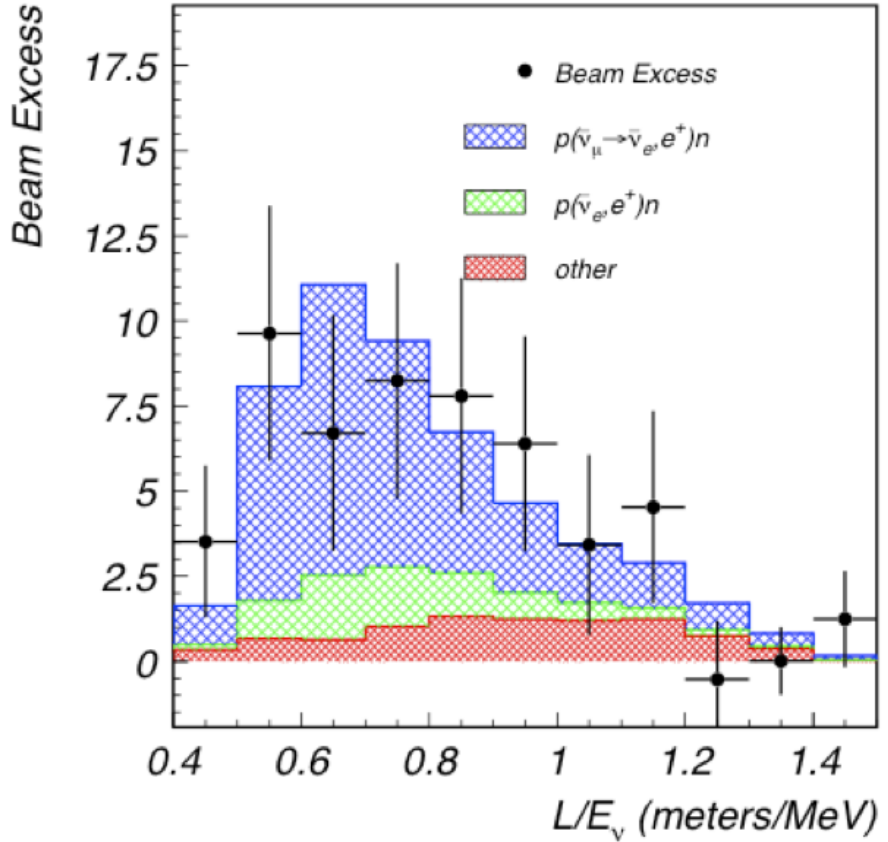


Figure 1.3.: The LSND excess as a function of the neutrino L/E value. Events require a positron in the energy range $20 < E < 60$ MeV and a likelihood ratio of > 10 that the associated gamma was correlated (i.e. $\frac{\mathcal{L}_\gamma(\text{correlated})}{\mathcal{L}_\gamma(\text{accidental})} > 10$) [8].

1.3.2. MiniBooNE

MiniBooNE collected data from the Booster Neutrino Beam (BNB) operating in both neutrino and anti-neutrino mode. The BNB is described in detail in Section 2.3. The (anti-)neutrinos had an energy range of $200 < E_\nu < 1250$ MeV and the baseline of the experiment was 541 m. Similar to LSND, MiniBooNE was searching for $(\bar{\nu}_e^-)$ appearance from a predominantly $(\bar{\nu}_\mu^-)$ beam. In neutrino mode, MiniBooNE observed an excess of 381.2 ± 85.2 Charged Current Quasi Elastic (CCQE) events which corresponds to a 4.5σ excess. This is shown in Figure 1.4. Combining this with the anti-neutrino data, an excess of 460.5 ± 99.0 CCQE events (4.7σ) were observed. A two neutrino model is assumed so

that a comparison with LSND data can be made, however this results in the appearance and disappearance data not being compatible with one another. This may be resolved by assuming a different model to the 3+1 neutrino framework. The results are consistent with those seen by LSND and again point to the existence of additional neutrino flavours beyond the three predicted by the SM [9].

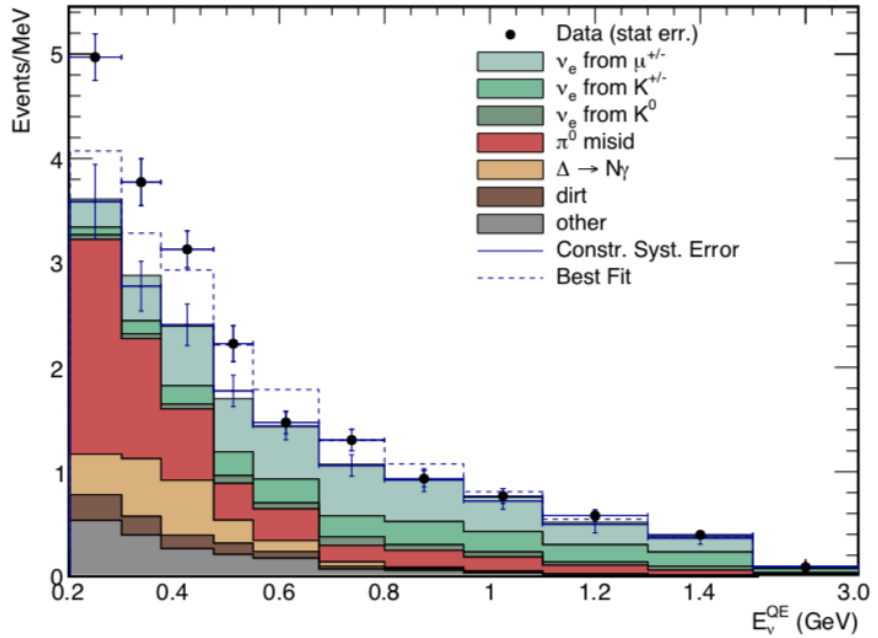


Figure 1.4.: The MiniBooNE excess from ν_e CCQE events. The best fit line assumed two neutrino oscillations [9].

1.3.3. Gallium Anomaly

The *Gallium Anomaly* refers to the apparent deficit of electron neutrinos observed by placing radioactive sources which decay via electron capture in the solar neutrino experiments, SAGE and GALLEX. The GALLEX experiment utilised two separate ^{51}Cr neutrino sources. The key measured quantity was the production of ^{71}Ge due to transformation of ^{71}Ga via inverse beta decay. The strength of the ^{51}Cr neutrino sources was measured directly and via the production of ^{71}Ge . The combined ratio of the strength of the two sources was found to be 0.93 ± 0.08 [10]. A later reanalysis of the results from GALLEX with new technical data gave a ratio of 0.902 ± 0.078 [11]. Similar to the GALLEX experiment, the SAGE experiment also compared the strength of a neutrino source from direct measurements and the production of ^{71}Ge . SAGE used both a ^{51}Cr and a ^{37}Ar source. SAGE observed a ratio 0.95 ± 0.12 for the ^{51}Cr source and a ratio of $0.79_{-0.10}^{+0.09}$ for the ^{37}Ar source. The weighted average from the results from the two sources from SAGE and the reevaluated values from the two GALLEX sources is 0.88 ± 0.05 [12]. This is consistent with a 2.3σ significance and is consistent with $\bar{\nu}_e$ disappearance due to mixing with a sterile neutrinos [40].

1.3.4. Reactor Anomaly

The *Reactor Anomaly* refers to the apparent deficit of anti-electron neutrinos produced from neutron rich fission products such as ^{235}U , ^{238}U , ^{239}Pu and ^{241}Pu undergoing β -decay. For most cases this involves placing a detector within a 100m of a reactor and measuring the ratio of observed to predicted event rates. The average ratio is 0.943 ± 0.023 . It is acknowledged that the reactor fluxes may not be perfectly understood which could be the cause for such a deficit, however it should be noted that other experiments have observed similar deficits for comparable L/E ranges [13].

1.3.5. Theoretical Motivation

Assuming that the mass generation of neutrinos follows similar rules to that of other particles, there is clear motivation to try and attempt to include sterile neutrinos into

theoretical models since right handed particles are typically required for mass generation. Some of the potential options for neutrinos mass generation are discussed in Section 1.4.1. The initial mass scale for sterile neutrinos is unconstrained, however one of the more well motivated models is the "Type 1" *Seesaw model* which attempts to explain the relative size of neutrino masses points towards very heavy sterile neutrino masses ($\gg 1$ eV). Variations of the Seesaw model have also been proposed that incorporate light sterile neutrinos [41].

1.4. Theory of Sterile Neutrinos

1.4.1. Neutrino Mass

The SM Lagrangian, L , for a fermion is given by

$$L = \bar{\psi}(i\gamma^\mu \partial_\mu - m)\psi \quad (1.23)$$

with the solution being the Dirac equation given by [22]

$$(i\gamma^\mu \partial_\mu - m)\psi = 0. \quad (1.24)$$

Dirac Mass

Within the SM Lagrangian, the Dirac mass term is given by $m_D \bar{\psi}\psi$ where ψ is the Dirac spinor. By dividing this into left and right components we have

$$\begin{aligned} m_D \bar{\psi}\psi &= m_D (\overline{\psi_L + \psi_R})(\psi_L + \psi_R) \\ &= m_D (\overline{\psi_L}\psi_R + \overline{\psi_R}\psi_L), \end{aligned} \quad (1.25)$$

where the second step follows from Equation 1.4. Naturally, to have a non-zero Dirac mass term, particles require a left and right handed chiral state. This is the mass generation method that all particles in the SM follow and hence why neutrinos are massless in the SM. To give the neutrino mass in this way, one could just introduce a field associated with a right handed neutrino. This would usually correspond to the left handed neutrinos

being the *active* ones, whilst the right handed neutrinos would be considered *sterile*. Since left handed particles form a doublet under SU(2) they have non-zero weak isospin and because right handed particles are a singlet under SU(2), their weak isospin is equal to zero. Therefore, in order to get a term where the isospin sums to zero, which is a requirement to be gauge invariant, an additional field is needed that is also a doublet under SU(2). This field is a result of the neutral Higgs boson, ϕ^0 , and the Dirac mass is given by

$$m_D = y\langle\phi^0\rangle = \frac{yv}{\sqrt{2}}, \quad (1.26)$$

where y is the Yukawa coupling and v gives the weak scale ($v \simeq 246$ GeV). A concern with generating neutrino masses in this way is the required size of the Yukawa coupling. To generate a mass of say 0.1 eV, the Yukawa coupling would need to be very small (~ 6 orders of magnitude less than that of the electron). This small number is sometimes considered unnatural and provides motivation to search for alternative mass mechanisms to explain the neutrino masses [22].

Majorana Mass

To generate mass without the requirement of a right handed field, it is required that the neutrino be a Majorana particle. It may be shown that

$$\psi_R = C\overline{\psi_L}^T, \quad (1.27)$$

where the superscript T indicates the transpose and $C = i\gamma^2\gamma^0$ which is the charge conjugation eigen value. By defining $\psi_L^C = C\overline{\psi_L}^T$, the Majorana field may then be written as

$$\psi = \psi_L + \psi_R = \psi_L + \psi_L^C. \quad (1.28)$$

Combining this with the mass term in Equation 1.23, the left handed Majorana mass term is given by

$$\frac{m_L}{2}(\overline{\psi_L}^C\psi_L + \overline{\psi_L}\psi_L^C), \quad (1.29)$$

where the factor of $1/2$ arises due to double counting. As before, in order to get the weak isospin to sum to zero the Higgs field needs to be introduced, but in this case a Higgs triplet (instead of doublet) is required. However, within the SM, a Higgs triplet isn't allowed and there doesn't seem to be any experimental evidence for one either [22].

Seesaw mechanism

In the general case, we have four neutrino fields, a left and right handed one plus a charge conjugate version of each. This allows us to create a left and right Majorana mass term akin to Equation 1.29 and a regular and charge conjugated Dirac mass akin to Equation 1.25 (the Dirac mass, m_D is the same in both cases). The mass component of the Lagrangian, L_{mass} , may be written as a matrix equation,

$$L_{mass} = \frac{1}{2} \begin{pmatrix} \overline{\psi}_L^C & \overline{\psi}_R \end{pmatrix} \begin{pmatrix} m_L & m_D \\ m_D & m_R \end{pmatrix} \begin{pmatrix} \psi_L \\ \psi_R^C \end{pmatrix} + h.c. \quad (1.30)$$

where the central 4×4 matrix is known as the mass matrix, \mathcal{M} . By diagonalising \mathcal{M} into mass eigenstates, m_1, m_2 , and assuming $m_L = 0$ (since it isn't allowed in the SM) and that $m_R \gg m_D$, the mass eigenstates may be expressed as

$$\begin{aligned} m_1 &\simeq \frac{m_D^2}{m_R} \\ m_2 &\simeq m_R. \end{aligned} \quad (1.31)$$

Since we have said that $m_R \gg m_D$, m_2 is also large and m_1 is small since the value of m_D^2 is suppressed by the large value of m_R in the denominator. Furthermore, the larger the value of m_2 , the smaller the value of m_1 . This linked relationship gives rise to the so-called *seesaw mechanism*. m_1 would give the mass scale of the active neutrinos whereas m_2 would be a heavy sterile neutrino. This mechanism requires neutrinos to be Majorana particles, but does provide an explanation on the relative smallness of the neutrino masses compared with other SM particles [22].

1.4.2. Sterile Neutrino Oscillations

An overview of the physics describing neutrino oscillations within the active sector was presented in Section 1.2.3. This approach may be extended to include an arbitrary number of additional neutrino states by expanding the PMNS matrix to include the desired number of sterile neutrinos

$$U_{\text{sterile}} = \begin{pmatrix} U_{e1} & U_{e2} & U_{e3} & U_{e4} & \dots \\ U_{\mu 1} & U_{\mu 2} & U_{\mu 3} & U_{\mu 4} & \dots \\ U_{\tau 1} & U_{\tau 2} & U_{\tau 3} & U_{\tau 4} & \dots \\ U_{s1} & U_{s2} & U_{s3} & U_{s4} & \dots \\ \vdots & \vdots & \vdots & \vdots & \ddots \end{pmatrix}. \quad (1.32)$$

For simplicity, often only the case with one sterile neutrino is considered. This is known as the (3 + 1) neutrino framework where we have the three usual active neutrinos with the addition of one sterile neutrino. Within a (3 + 1) framework and assuming that $\Delta m_{41}^2 \gg |\Delta m_{31}^2|, \Delta m_{21}^2$, short baseline oscillation are well represented by the two flavour oscillation probability,

$$P_{\nu_\alpha \rightarrow \nu_\beta} = \delta_{\alpha\beta} - 4|U_{\alpha\beta}|^2(\delta_{\alpha\beta} - |U_{\alpha\beta}|^2)\sin^2\left(\frac{\Delta m_{41}^2 L}{4E}\right), \quad (1.33)$$

where $\delta_{\alpha\beta}$ is the Kronecker delta between states α and β , $U_{\alpha\beta}$ are the relevant entries from the PMNS matrix and Δm_{41}^2 is the mass splitting involving the sterile neutrino state [42].

When performing a search for sterile neutrinos, typically there are three channels, one or more of which may be probed (plus their corresponding anti-neutrino variants). For each of these channels, the relevant PMNS matrix elements are parameterised in terms of

mixing angles such that,

$$\nu_\mu \text{ disappearance } (\nu_\mu \rightarrow \nu_\mu) : \sin^2 2\theta_{\mu\mu} \equiv 4|U_{\mu 4}|^2(1 - |U_{\mu 4}|^2) \quad (1.34)$$

$$\nu_e \text{ appearance } (\nu_\mu \rightarrow \nu_e) : \sin^2 2\theta_{\mu e} \equiv 4|U_{\mu 4}|^2|U_{e 4}|^2 \quad (1.35)$$

$$\nu_e \text{ disappearance } (\nu_e \rightarrow \nu_e) : \sin^2 2\theta_{ee} \equiv 4|U_{e 4}|^2(1 - |U_{e 4}|^2). \quad (1.36)$$

It should be noted that ν_e appearance depends on $U_{\mu 4}$ and $U_{e 4}$, which ν_μ and ν_e disappearance depend on respectively. The observation of ν_e appearance would therefore automatically imply that ν_μ and ν_e disappearance is also present. Additionally, this allows these parameters to be over constrained [42]. The current global best fit values for the three mixing angles and the mass splitting term, Δm_{41}^2 are outlined in Table 1.4.2.

Oscillation Parameter	Best Fit Value
$\sin^2 2\theta_{\mu\mu}$	0.07157
$\sin^2 2\theta_{\mu e}$	0.0009809
$\sin^2 2\theta_{ee}$	0.05310
Δm_{41}^2	1.32

Table 1.2.: The global best fit values for the (3 + 1) sterile neutrino oscillation parameters. [37]

Chapter 2.

The Short Baseline Neutrino Program

2.1. SBN Program Overview

The SBN program is comprised of three distinct Liquid Argon Time Projection Chamber (LArTPC) type detectors located at Fermilab. The three detectors are Short Baseline Near Detector (SBND), Micro Booster Neutrino Experiment (MicroBooNE) and Imaging Cosmic and Rare Underground Signals (ICARUS) and all three lie along the axis of the BNB. In order to minimise systematic uncertainties, the three detectors share many of the same technologies, the details of which are discussed in Section 2.5 (SBND), Section 2.6 (MicroBooNE) and Section 2.7 (ICARUS). The BNB consists predominantly of muon neutrinos with energies of the order 1 GeV and is discussed in detail in Section 2.3. The three detectors are positioned at 110m, 470m and 600m from the neutrino beam source respectively [42].

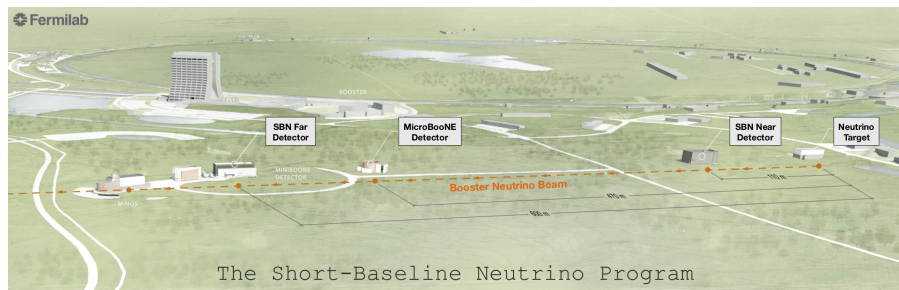


Figure 2.1.: A view of the Fermilab complex highlighting the position of the SBN detectors [42].

One of the primary aims of the SBN program is to provide a definitive test to either confirm or refute the existence of light sterile neutrinos which have been hinted at by a number of experiments discussed in Section 1.3. Other major aims of the SBN program include investigating neutrino argon cross sections and developing large scale LArTPC technologies. The close proximity of SBND to the BNB source means that SBND will observe neutrino argon interactions with high statistics allowing statistical uncertainties to be minimised and will allow for the exploration of rare channels such as neutrino-electron scattering. Both the development of LArTPC technology and an improved understanding of neutrino interaction cross-sections will be invaluable for future neutrino experiments such as the Deep Underground Neutrino Experiment (DUNE) [42].

2.2. Liquid Argon Time Projection Chambers

The idea of a LArTPC was first proposed in 1977 by Rubbia in an attempt to consolidate the high resolution but low number of interactions obtained from 'bubble chamber' style detectors and the high rate but low resolution interactions obtained from 'counter' experiments. This would be achieved by propagating the complete image of an event through a noble element and then electronically reconstructing the 3D event by combining the 2D information collected and the drift time [43].

Liquid argon was identified as the most suitable medium to use for such a detector due to the following properties [43];

- High density (1.4 gcm^{-3}) with a sufficiently high atomic mass to allow for a reasonable probability of neutrino interactions.
- Argon is a noble element, meaning the electrons will not combine with the argon resulting in long drift times.
- A high electron mobility, meaning the electrons may drift quickly across the detector.
- Argon is relatively cheap and easy to purify.
- Argon may be liquefied easily using liquid nitrogen.

2.2.1. LArTPC Design

The general design of a single chamber LArTPC is shown in Figure 2.2. Most LArTPCs consist of one or more Time Projection Chambers (TPCs) with a cathode and anode plane at either end inducing an electric field across the TPC. The electric field causes charged particles to drift in the detector. The electrons produced from neutrino interactions will drift towards the anode where they will induce a current on a series of wire planes. The most rear wire plane (the one furthest away from the cathode) is known as the collection plane and the one or more wire planes in front of the collection plane are known as induction plane(s). There is a further potential difference between the induction and collection planes which ensures that the electrons will also reach the collection plane. The wire planes are orientated so that the wire angles between the planes are different which allows for 2D position reconstruction. Located behind the anode plane are also a series of PMTs which collect scintillation light. The time taken for the scintillation light to be detected is very short in comparison to the time taken for the electrons to drift to the wire planes, so by using this timing information and knowing the electron drift velocity, the horizontal drift distance may be determined. Combining this with the 2D information from the wire planes allows for 3D event reconstruction. The induced current on the wire planes is interpreted in terms of signal waveforms from which *hits* are constructed. Each hit contains information such as the associated wire plane, wire number and charge and it is this information which is used to obtain reconstructed information about an event [44]. The specific designs of the three LArTPCs used in the SBN program are discussed in Section 2.5 (SBND), Section 2.6 (MicroBooNE) and Section 2.7 (ICARUS).

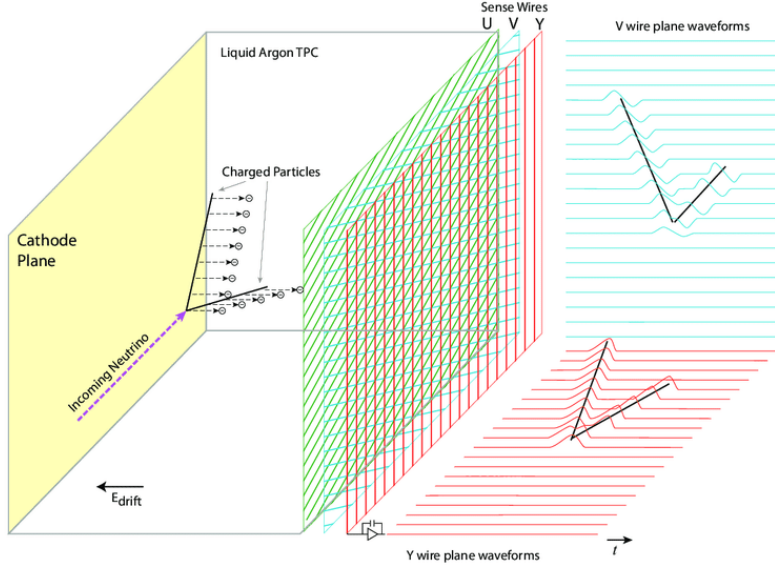


Figure 2.2.: A schematic of the operating principle of a LArTPC detector. A neutrino interacts in the argon producing secondary particles. The electric field across the TPC causes charged particles to drift towards the wire planes where their energy deposits are recorded. [44]

2.2.2. Detector effects

Despite the many desirable properties of liquid argon, there are still a number of effects which have to be considered when performing event reconstruction.

Diffusion

Diffusion is the process in which the drifting electrons do not drift in such a way that they will continue to perfectly represent the initial image of an event. That is to say that the electrons will disperse as they drift in the detector. This happens in both the transverse and longitudinal directions with respect to the direction of the electric field and impacts the spatial resolution of the detector [45].

For the case of a zero electric field and with the electrons in thermal equilibrium, the diffusion is isotropic and the diffusion coefficient, D , is given by the Einstein relation such

that

$$D = \frac{kT}{e} \mu_0, \quad (2.1)$$

where k is Boltzmann's constant, T is the temperature, e is the elementary charge and μ_0 is the electron mobility (for the case of no electric field) [45].

In the presence of an electric field, the electron mobility is no longer given by μ_0 , but instead by μ and the electrons are no longer in thermal equilibrium. The diffusion also becomes anisotropic, leading to distinct diffusion coefficients for the longitudinal and transverse directions, D_L and D_T respectively which are given by

$$\begin{aligned} D_L &= \frac{kT}{e} \left(\mu + E \frac{\partial \mu}{\partial E} \right) \\ D_T &= \frac{kT}{e} \mu. \end{aligned} \quad (2.2)$$

In general, the diffusion in the transverse direction is greater than the diffusion in the longitudinal direction [45] [46].

Electron Lifetime

Electron lifetime is a measure of the free electrons lost due to attachment to impurities in the liquid argon whilst drifting across the detector [47]. Naturally, the electron lifetime, τ_e , is coupled to the purity of the argon and is defined as

$$\tau_e = 1/k_e, \quad (2.3)$$

where k_e is the impurity concentration. The rate of charge loss is then given by

$$Q = Q_0 e^{-t/\tau_e}, \quad (2.4)$$

where Q is the charge remaining after correcting for electron lifetime, Q_0 is the initial charge and t is the drift time [47].

Recombination

When argon atoms are ionised, the resulting ionised electron may immediately recombine with a nearby argon ion instead of being separated by the electric field in the detector. This is known as the recombination effect and the magnitude of the effect is largely determined by the local electric field. A number of different approaches to model the recombination effect exist, however for liquid argon detectors a form of the box model or Jaffé model are usually used [45].

The Jaffé model is based on the idea that recombination depends on the charge density of both nearby electrons and ions. The model assumes a cylinder surrounding the ionisation track and recombination may occur between any of the ionised electrons and ions, not just the electron with its associated parent ion which is where the Jaffé model largely differs from earlier models [48]. The recombination effect from the Jaffé model is given by

$$Q = \frac{Q_0}{1 + q_0 F(E \sin \phi)}, \quad (2.5)$$

where Q_0 is the initial charge, Q is the charge after recombination, q_0 is the initial density of electron-ion pairs and F is a function depending on the electric field E , the angle between the field and the ionisation track, ϕ and other quantities which describe the diffusion. Equation 2.5 is commonly approximated by Birks' law with a normalisation parameter to help fit the model to the experimental data [45].

In their development of the box model, Thomas and Imel assumed the diffusion and ion mobility to be zero and instead of the cylindrical column used in the Jaffé model, they considered a box with a uniform charge distribution such that,

$$Q = Q_0 \frac{1}{\xi} \ln(1 + \xi), \quad (2.6)$$

where $\xi = \alpha Q_0 / E$. α is a free parameter and Q and Q_0 are defined as in Equation 2.5 [45] [49].

Space Charge

The electric field in a TPC is usually designed to be uniform between the cathode and the anode, however, particularly for surface level detectors this often doesn't end up being the case. Cosmic muons may enter the detector ionising the argon atoms. The ionised electrons and argon ions then drift towards the anode and cathode respectively, however the drift time for the ions is much greater than the electron drift time. If the flux of cosmic muons entering the detector is sufficiently large, this results in a significant positive charge build up towards the cathode. This effect is known as *space charge* and directly impacts the recombination effect since it is linked to the magnitude of local electric field as well as affecting the drifting electrons [50].

The ion drift velocity, \vec{v} , is given by

$$\vec{v} = \mu \vec{E}, \quad (2.7)$$

where μ is the ion mobility and \vec{E} is the electric field. The build up of charge density, ρ , is given by the continuity equation,

$$\vec{\nabla} \cdot \vec{J} + \frac{\partial \rho}{\partial t} = K, \quad (2.8)$$

where $\vec{J} = \rho \vec{v}$ and K is the volume rate at which ion pairs are created ([K] = ion pairs/volume/second) [51].

With the simplified assumption that the build up of charge is constant (time-independent) and that the drift direction is only in the x direction which is the same as the electric field, Equation 2.8 may be reduced to

$$\frac{d\rho v}{dx} = K. \quad (2.9)$$

Gauss's law states that,

$$\nabla \cdot \vec{E} = \frac{\rho}{\epsilon}, \quad (2.10)$$

where ϵ is the dielectric constant of the medium. By combining Equation 2.9 and Equation 2.10 it follows that

$$\frac{dE}{dx} = \frac{Kx}{\mu E \epsilon}. \quad (2.11)$$

By defining the coordinates of the system such that the anode is at $x = 0$ and $0 \leq x \leq D$ where D is the position of the cathode, Equation 2.11 may be integrated via,

$$\int_{E_A}^E E' dE' = \int_0^x \frac{Kx'}{\mu \epsilon} dx', \quad (2.12)$$

where E_A is the electric field at the anode and both E' and x' are dummy variables. This gives an x dependent electric field solution,

$$E(x) = \sqrt{E_A^2 + \frac{Kx^2}{\mu \epsilon}} = E_0 \sqrt{\left(\frac{E_A}{E_0}\right)^2 + \alpha^2 \frac{x^2}{D^2}}, \quad (2.13)$$

where $E_0 = V/D$ is the nominal electric field, V is the difference in the voltage between the anode and cathode and $\alpha = \frac{D}{E_0} \sqrt{\frac{K}{\epsilon \mu}}$ which is a dimensionless parameter [51].

2.3. Booster Neutrino Beam

The BNB is produced by firing 8 GeV protons onto a beryllium target resulting in a secondary beam of hadrons [52]. A toroidal focusing horn surrounds the target and focuses or defocuses charged particles depending on the sign of their charge. The focused hadrons then travel down a 50 m tunnel where most of them will decay producing muon neutrinos and small fraction of electron neutrinos. At the end of the 50 m decay region is a concrete and steel absorber designed to absorb any non-neutrino particles [53]. A schematic of the BNB layout is shown in Figure 2.3. The decay modes of the hadrons resulting in a neutrino and the corresponding branching ratios are listed in Table 2.1.

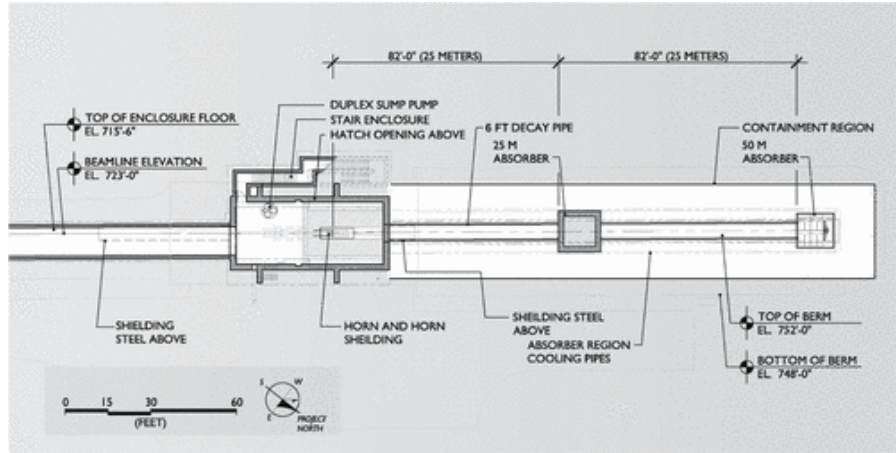


Figure 2.3.: A schematic of the layout of the BNB [54].

Particle	Decay Mode	Branching Ratio (%)
π^+	$\mu^+ + \nu_\mu$	99.9877
	$e^+ + \nu_e$	0.0123
k^+	$\mu^+ + \nu_\mu$	63.44
	$\pi^0 + e^+ + \nu_e$	4.98
	$\pi^0 + \mu^+ \nu_\mu$	3.32
k^0	$\pi^- + e^+ + \nu_e$	20.333
	$\pi^+ + e^- + \bar{\nu}_e$	20.197
	$\pi^- + \mu^+ + \nu_\mu$	13.551
	$\pi^+ + \mu^- + \bar{\nu}_\mu$	13.469
μ^+	$e^+ + \nu_e + \bar{\nu}_e$	100

Table 2.1.: The decay modes of the hadrons produced by the BNB when running in neutrino mode. The branching ratio of each of the decay modes is also given [54].

A current of 174 kA is supplied to the magnetic horn in 143 μ s pulses which corresponds to the frequency of the incident protons. The direction of the current may be reversed allowing for the focusing of positively or negatively charged particles. Since the charge of the decaying hadrons is linked to the type of neutrino produced, the ability to focus both positively and negatively charged particles allows the BNB to run in neutrino or anti-neutrino mode [54]. Pions are the primary particle produced from the incident protons

hence the BNB is muon (anti-)neutrino dominated. The percentage neutrino flavour composition of the BNB is given in Table 2.2 for both neutrino and anti-neutrino mode.

Neutrino Flavour	% in Neutrino Mode	% in Anti-neutrino Mode
ν_μ	93.6	15.71
$\bar{\nu}_\mu$	5.86	83.73
ν_e	0.52	0.2
$\bar{\nu}_e$	0.05	0.4

Table 2.2.: The neutrino flavour composition of the BNB when it's running in either neutrino or anti-neutrino mode [54].

The neutrino flux of the BNB was simulated by the MiniBooNE collaboration for both neutrino and anti-neutrino mode [54]. The flux of the electron and muon (anti-)neutrinos in each of the three SBN detectors is shown in Figure 2.4. The systematic uncertainties

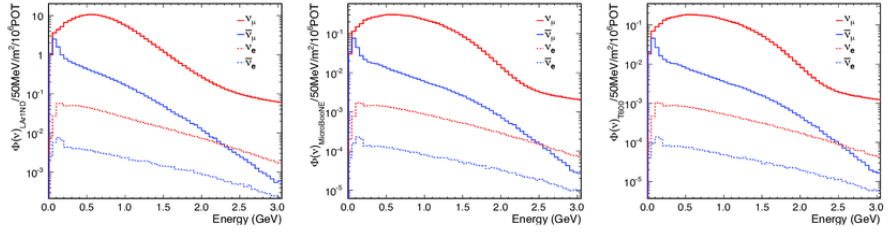


Figure 2.4.: The predicted flux of the BNB at SBND (left), MicroBooNE (middle) and ICARUS (right) for both electron and muon neutrinos and anti-neutrinos [55].

associated with the BNB account for an error of $\sim 9\%$ at the peak of the ν_μ flux with a larger error for energies either side of the peak. The systematic uncertainties are mainly due to determining the rate and spectrum of neutrinos for each proton on target, determining the rate and spectrum of secondary particles produced from protons interacting with the beryllium target, the rate of hadronic interactions, the focusing properties of the magnetic horn and the beamline geometry [54].

2.4. Neutrino Interactions

The following section outlines some of the most common CC and NC interaction processes in SBN. The associated CC and NC Feynman diagrams for these processes are shown in Figure 2.6 and Figure 2.7 respectively. Only examples of neutrino interactions are shown, however, these may be easily adapted to the anti-neutrino case. Additionally, interaction flavours are kept general with l representing the lepton flavour. In principle $l \in \{e, \mu, \tau\}$, however, within SBN only the electron and muon flavours are relevant.

Elastic and Quasi-Elastic

When particles interact via elastic scattering, energy is conserved and the initial particles do not change. Since neutrinos are neutral particles that weakly interact, NC elastic scattering being mediated by the Z^0 boson may occur with a neutrino scattering off a proton via

$$\nu_l + p \rightarrow \nu_l + p. \quad (2.14)$$

Quasi-elastic scattering is similar to elastic scattering, however charge is exchanged and therefore the interaction is mediated by the W^+ boson. In these interactions the incoming neutrino scatters off a neutron and is converted to its charged lepton counterpart whilst the neutron changes to a proton via

$$\nu_l + n \rightarrow l^- + p. \quad (2.15)$$

CCQE interactions are the most abundant in the GeV range, which is the energy range of the BNB [56].

Resonant

At higher energies, the neutrino-nucleon interaction may cause the nucleon to be excited into a Delta resonance (Delta baryon). The Delta resonance will then decay back into a

nucleon plus a pion. For CC interaction this occurs via

$$\nu_l + N \rightarrow l^- + \Delta \rightarrow l^- + N + \pi, \quad (2.16)$$

whereas for NC interactions this occurs via,

$$\nu_l + N \rightarrow \nu_l + \Delta \rightarrow \nu_l + N + \pi. \quad (2.17)$$

In both cases, N represent some nucleon with Δ and π being one of the possible Delta resonances and pions appropriate for a given interaction [56] [57].

Meson Exchange Current

Bound nucleon pairs may be thought of as being bound due to the exchange of virtual mesons. This exchange of mesons is known as a MEC. In this type of interaction, multiple nucleons are excited in a quasi-elastic fashion. The boson may couple to either a nucleon or the meson that's being exchanged. This leads to a number of possibilities; 1) the boson couples to the exchanged meson (pion-in-flight diagram), 2) the boson couples at the vertex between the nucleon and exchanged pion (seagull diagram), 3) the meson exchange occurs with a virtual intermediate nucleon to which the boson couples, 4) as in case 3), but the intermediate particle is a Delta resonance instead of a nucleon. Feynman diagrams of the 4 possibilities are shown in Figure 2.5 with the MEC diagrams shown in Figure 2.6 and Figure 2.7 being generic examples of the interaction [56] [58] [59].

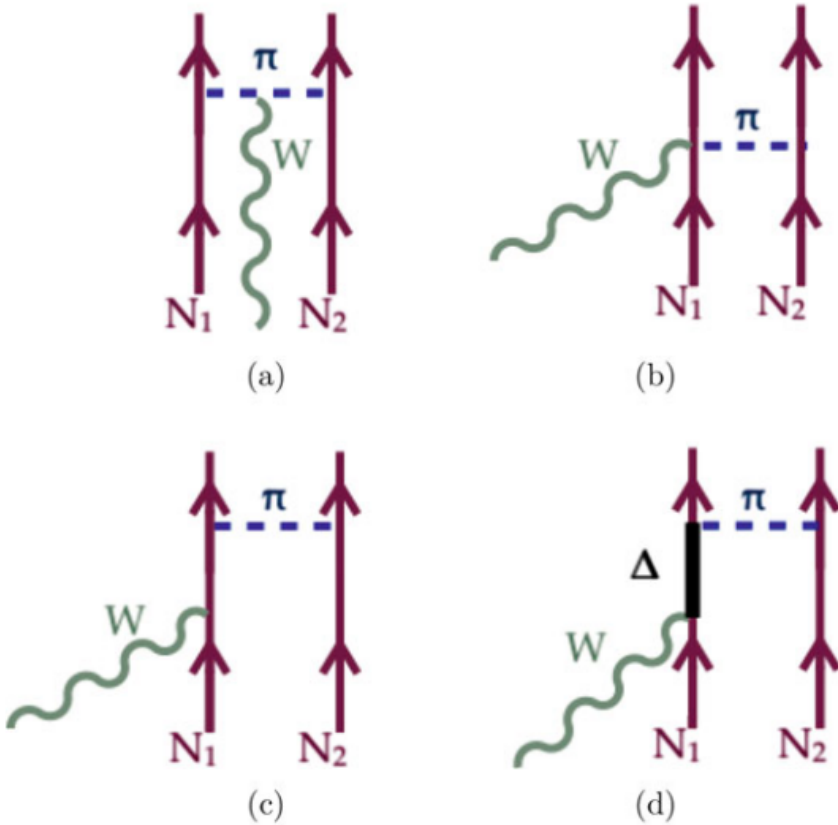


Figure 2.5.: Feynman diagrams of possible MEC interactions. The boson may couple to (a) the pion-in-flight, (b) the MEC vertex (seagull diagram), (c) an intermediate nucleon, (d) an intermediate Delta resonance [56].

Deep Inelastic Scattering

At even higher energies than those for resonant interactions ($> \mathcal{O}(5 \text{ GeV})$), Deep Inelastic Scattering (DIS) interactions become dominant. In DIS interactions, the neutrino scatters off individual quarks rather than the nucleon as a whole. This results in the break-up of the nucleon, but since the strong force prevents single quarks from existing a hadronic shower X , is produced [22] [56]. A CC DIS interaction occurs via

$$\nu_l + N \rightarrow l^- + X, \quad (2.18)$$

whereas the NC interaction occurs via

$$\nu_l + N \rightarrow \nu_l + X. \quad (2.19)$$

Coherent

Coherent interactions occur when the neutrino scatters off the whole nucleus with a negligible momentum transfer. This results in a pion being produced, but leaves the target nucleus unaltered. Coherent scattering may occur for both CC and NC interactions via

$$\nu_l + A \rightarrow l^- + A + \pi^+ \quad (2.20)$$

and

$$\nu_l + A \rightarrow \nu_l + A + \pi^0 \quad (2.21)$$

respectively [57] [58].

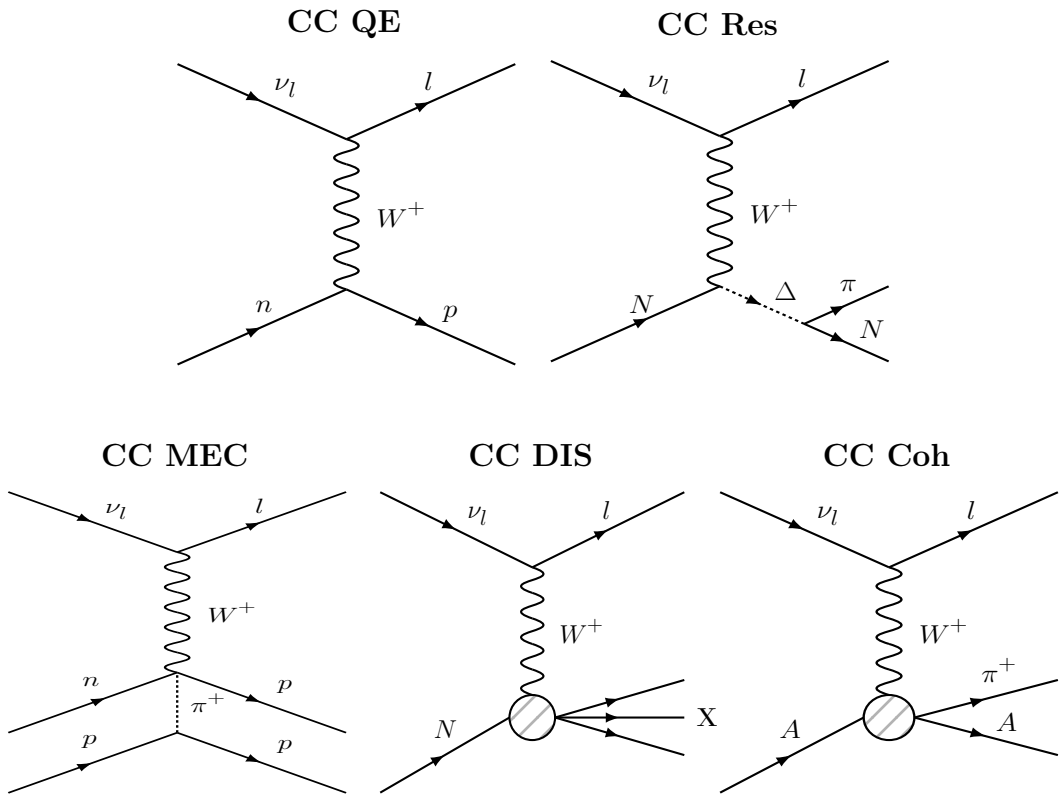


Figure 2.6.: Feynman diagrams of the CC processes most commonly expected in SBN. ν_l corresponds to the neutrino with leptonic flavour l , with l typically being either an electron or a muon. Δ denotes one of the possible Delta resonances, N denotes a nucleon, X denotes some set of final hadrons and A denotes a nucleus.

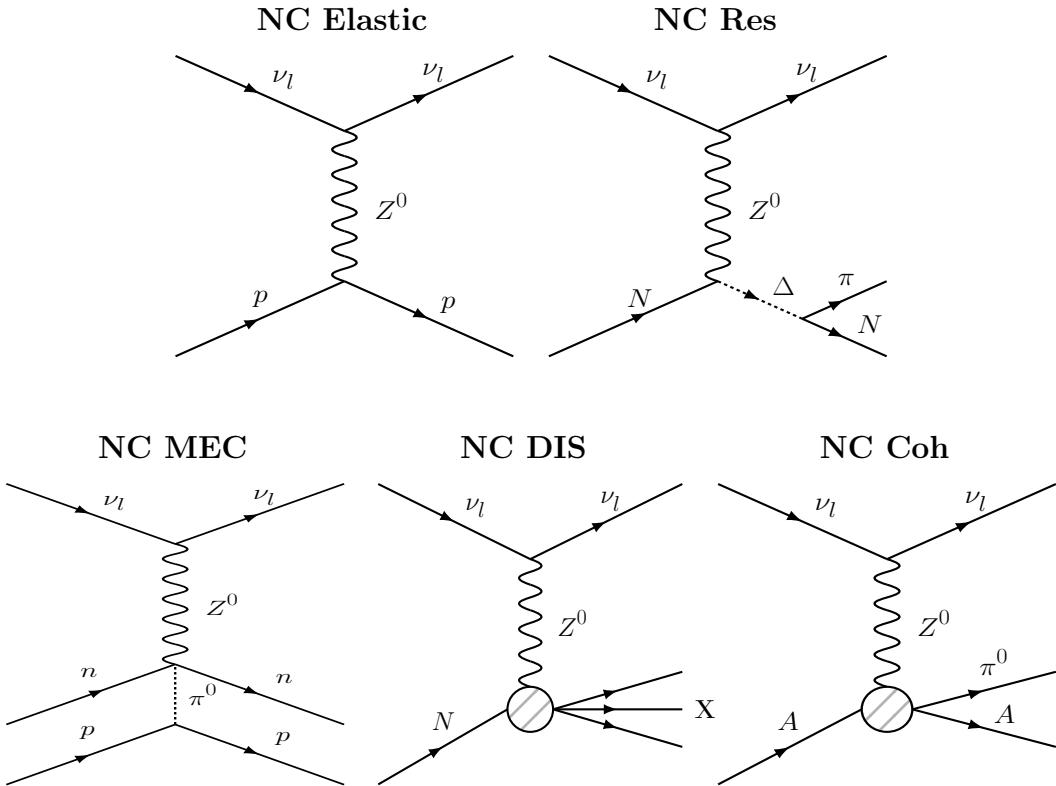


Figure 2.7.: Feynman diagrams of the NC processes most commonly expected in SBN. ν_l corresponds to the neutrino with leptonic flavour l , with l typically being either an electron or a muon. Δ denotes one of the possible Delta resonances, N denotes a nucleon, X denotes some set of final hadrons and A denotes a nucleus.

FIGURE SHOWING THE TOTAL (+ BREAKDOWN) NEUTRINO CC CROSS-SECTION AS A FUNCTION OF ENERGY. IS THERE AN UPDATED VERSION THAT INCLUDES MEC? - CAN'T FIND ONE ONLINE.. IS THERE A NC VERSION TOO?

2.5. SBND

DETAILS ON FIDUCIAL VOLUMES ETC.

SBND was purposely designed to be the near detector of the SBN program and has an active volume with dimensions (4, 4, 5) m containing 112 tons of liquid argon. It consists

of two TPCs, where the central shared cathode sits in the middle of the detector with an anode either side as is shown in Figure 2.8. Each of the Andode Plane Assemblys (APAs) consist of three wire planes where the first and second induction plane are orientated at $\pm 60^\circ$ to the vertical and the collection plane is vertical. In all cases, the wire plane spacing and the wire pitch are 3 mm. The nominal electric field in each of the TPCs is 500 V/m [55].

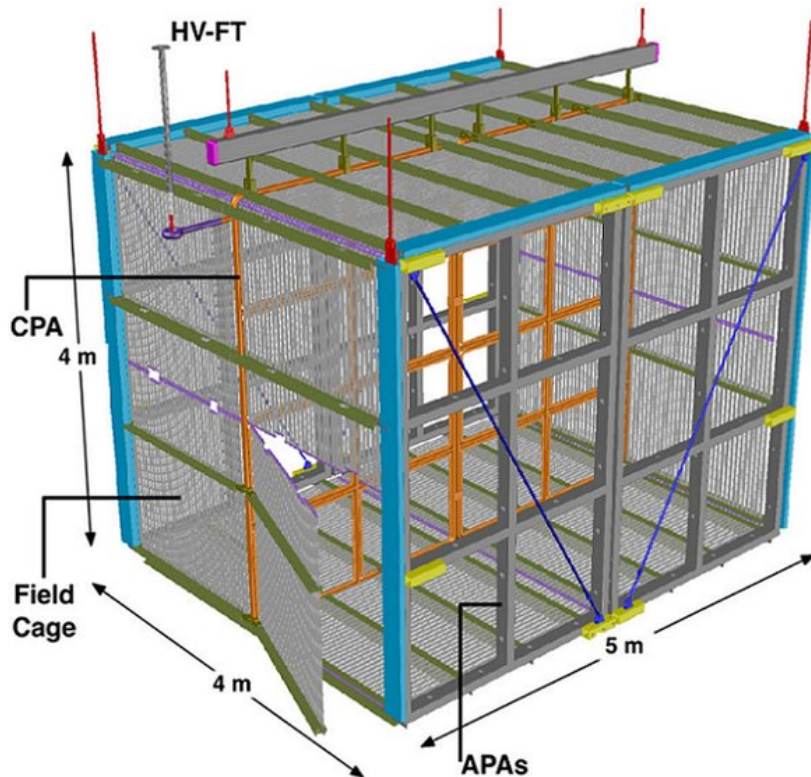


Figure 2.8.: Schematic showing the dimensions of the SBND detector. The Cathode Plane Assembly (CPA), APAs (only one is labelled) and field cage are shown. The Photon Detection System (PDS) is not shown, but 12 squares on the near APA represent the location where the PDS boxes will be positioned. [60]

Cosmic Ray Tagger

SBND is considered to be a surface level detector with no overburden. Consequently, the cosmic ray flux will be significant with an average of 3 cosmic rays seen in each neutrino

event [55]. This will be the most abundant background in SBND and therefore it will be crucial to be able to identify the cosmic ray muons. In order to do this, SBND will use a Cosmic Ray Tagger (CRT) system which consists of a total of 7 panels, one for each side of the detector plus an additional one for the top face as this is where most of the cosmic rays will be entering the detector from. Figure 2.9 shows how the CRT panels will be positioned. Each CRT plane consists of two layers, where one layer is comprised of 2×5 X-oriented modules and the other layer is comprised of 2×4 Y-oriented modules. Each of these modules is comprised of 16 scintillator strips which are in turn attached to Silicon Photomultipliers (SiPMs). The orthogonal two layer setup coupled with the SiPM readout allows the location of an interaction in the CRT to be determined [61]. The CRT system monitors the crossing time and coordinates of the particles and compares them with the information from the light detection system and the beam time rejecting the events identified as cosmic muons. [62].

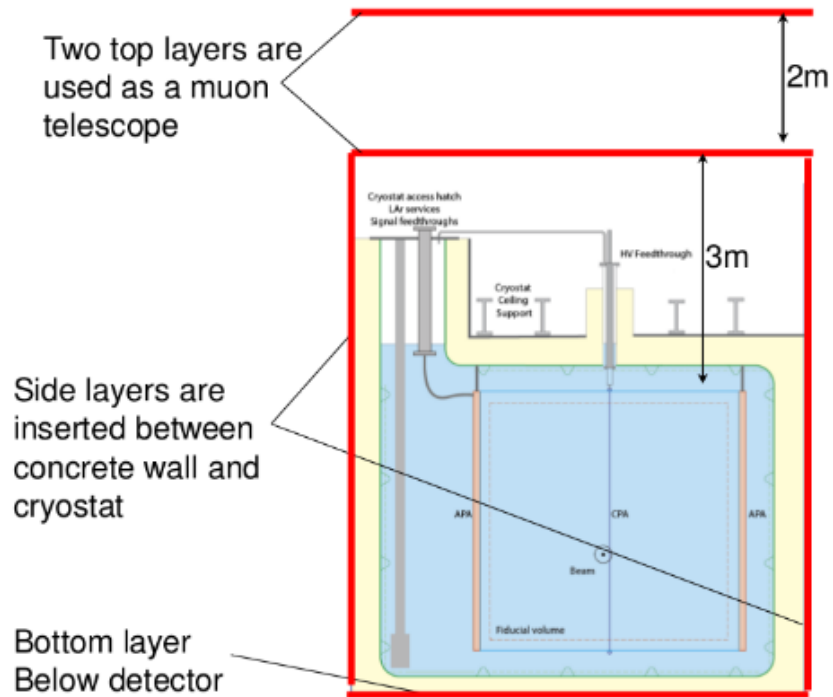


Figure 2.9.: Diagram showing how the CRT will surround SBND on all sides with an additional panel above the top surface [55].

READOUT ELECTRONICS?? KNOW LITERALLY NOTHING ABOUT THIS..

Photon Detection System

The PDS consists of a total of 24 *boxes*, 12 of which will be mounted behind each APA. Each box houses 5 PMTs and 8 Argon R&D Advanced Program at UniCamps (ARAPUCAs) (specifically, X-ARAPUCA's are used which are an advancement over the initial ARAPUCA design) as shown in Figure 2.11. The 4 outer PMTs of each box are coated with Tetraphenyl Butadiene (TPB) whilst the central one remains uncoated. The scintillation light produced has wavelengths in the Vacuum Ultra Violet (VUV) region, however the PMTs are only able to detect visible light. The TPB coating shifts the wavelength of the VUV light into the visible region allowing it to be detected. Therefore, the coated PMTs are sensitive to both visible and VUV light whilst the uncoated PMTs are only sensitive to visible light [60].

ARAPUCAs are a novel light trap which consist of a box where the internal surfaces are highly reflective. The surface of the ARAPUCA which faces the incoming light consists of dichroic filter with a wavelength shifter either side of the filter. The wavelength of the light which is incident on the outermost shifter is shifted such that it may pass through the dichroic filter and after passing through the filter the light is again wavelength shifted so that it may no longer pass through the filter and thus remains trapped in the ARAPUCA. A schematic of the ARAPUCA design is shown on the left of Figure 2.10. The inside of the ARAPUCA module contains a SiPM photo-sensor in order to detect the light. Due to the highly reflective nature of the inside of the ARAPUCA, only a small region needs to be exposed to a photo-sensor in order to detect the trapped photons [63]. The X-ARAPUCA improves on the initial design by replacing the inner wavelength shifter with an acrylic slab with the wavelength shifter implanted in the slab and the photo-sensor being directly attached to the slab. Light entering the X-ARAPUCA may be detected in same way as was done in the original ARAPUCA (Figure 2.10: Left), however the photons may also become trapped in the slab by total internal reflection and travel within the slab to the photo-sensor (Figure 2.10: Middle) or if the light enters at a large angle, the photons may become trapped between the surface of the slab and the filter and will travel to the photo-sensor without ever entering the slab (Figure 2.10: Right). The middle scenario of Figure 2.10 represents a direct improvement over the original ARAPUCA design because

the number of reflections on the internal sides of the X-ARAPUCA module is reduced which in turn increases the photon detection efficiency [64].

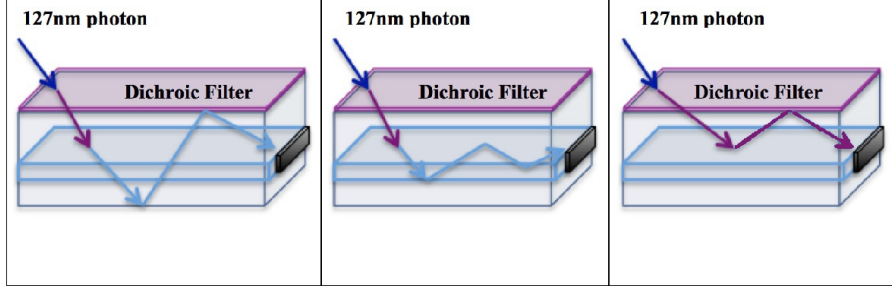


Figure 2.10.: The three possibilities for trapping light in an X-ARAPUCA. Left: The standard ARAPUCA design. Light is wavelength shifted in order to pass through the dichroic filter. Once passed the filter, it is wavelength shifted again so that may not exit through the filter again. The photons are reflected within the ARAPUCA until they are detected by the photo-sensor. Middle: an acrylic slab containing the inner wavelength shifter is placed in the X-ARAPUCA and the photo-sensor is attached to the slab. Light may become trapped within the slab by total internal reflection. Right: Incident light at a large angle may become trapped between the surface of the slab and the filter [64].

Another component of the PDS is covering each side of the CPA with a 19 m^2 of TPB coated reflective covering. This means that VUV light directed towards the CPA will be wavelength shifted into the visible spectrum and reflected back to towards the PMTs where it may be detected. Since one of the PMTs in each of the boxes remains uncoated, it will allow SBND to distinguish between light that is initially directed towards the PMTs and the reflected light because the reflected light will be visible in all PMTs whereas only the four outer PMTs will be able to detect direct light [60].

2.6. MicroBooNE

The MicroBooNE detector is located slightly upstream of its predecessor, MiniBooNE. The detectors are at 470 m and 541 m from the BNB source respectively. The Principal design goal of MicroBooNE is to investigate the low energy excess of events observed by MiniBooNE and it began its operations in 2015 were it was initially used as a stand alone detector before becoming part of the larger SBN program [65].

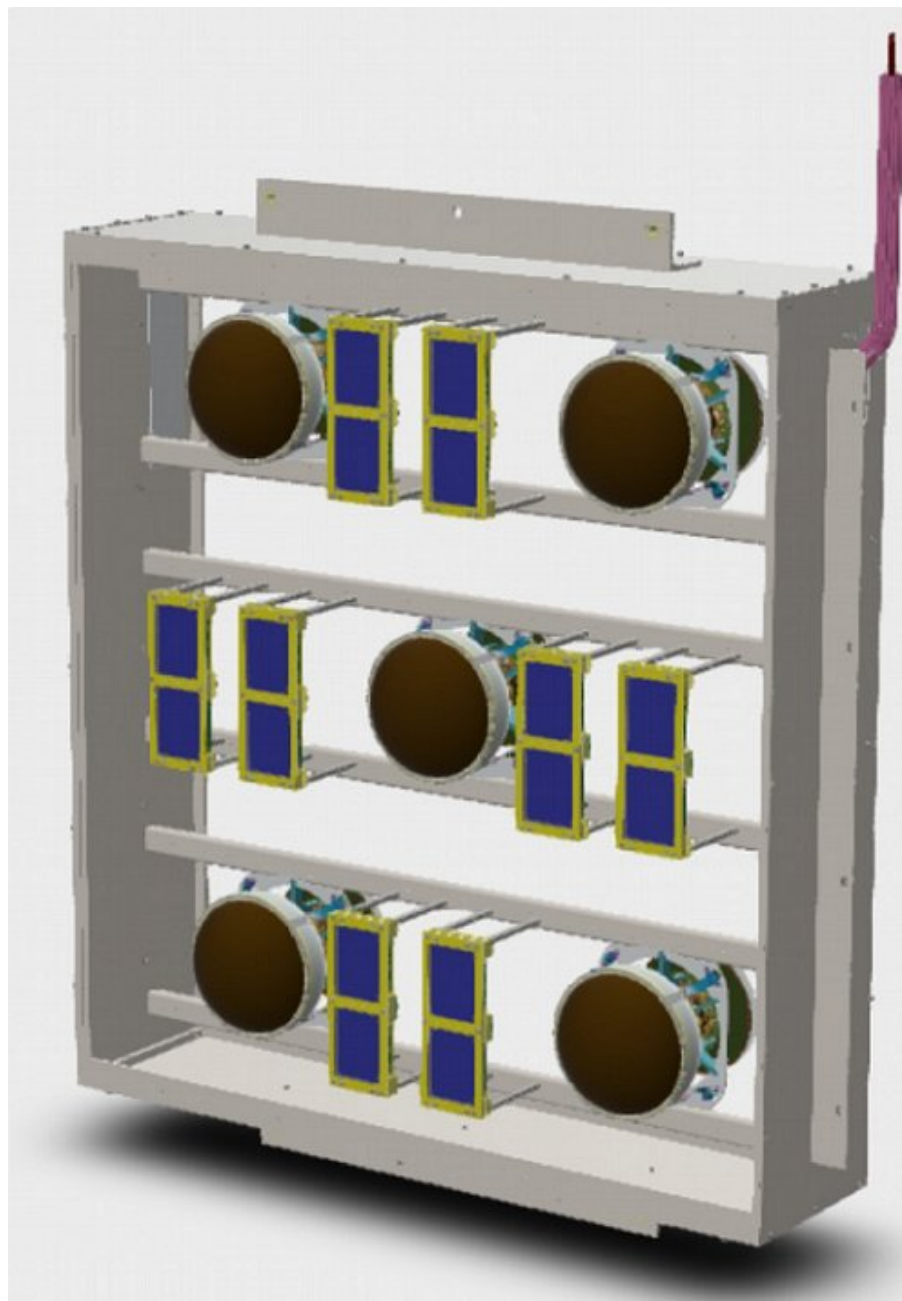


Figure 2.11.: Schematic of the PDS box showing the position of the 5 PMTs and the 4 pairs of X-ARAPUCA'S. The central PMT is left uncoated, whilst the 4 outer PMTs are coated with TPB [60].

The MicroBooNE detector consists of a single TPC enclosed within a cryostat as is shown in Figure 2.12. The TPC has dimensions of (2.560, 2.325, 10.368) m and is

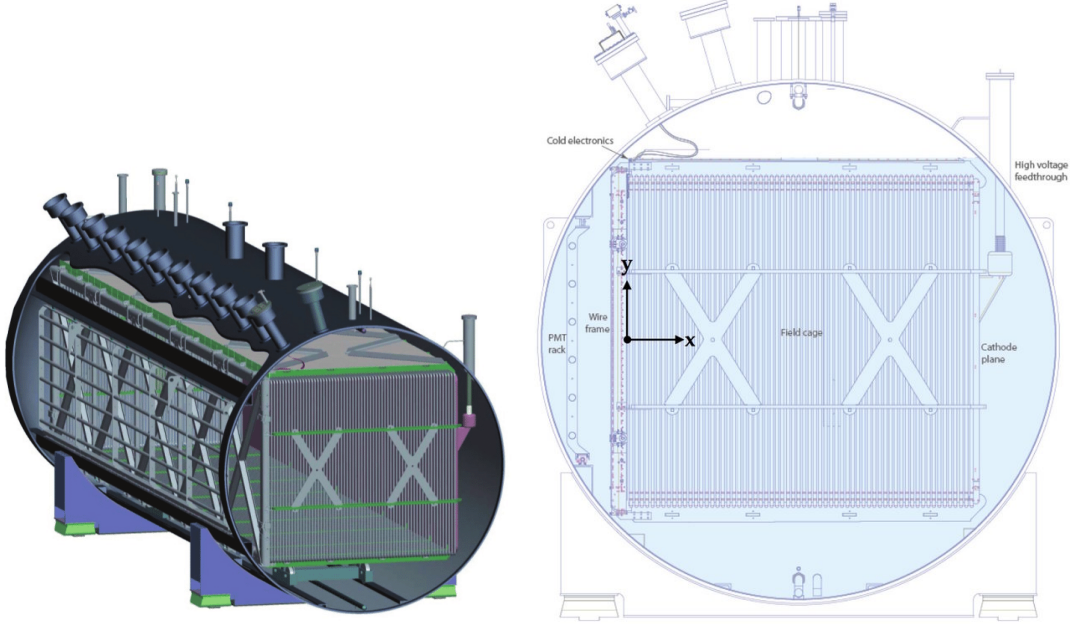


Figure 2.12.: Diagram of the MicroBooNE LArTPC inside the cryostat with the open front and left side showing the field cage and anode planes respectively (Left). Cross-section schematic of the MicroBooNE detector orientated such that the beam direction (z-direction) is orientated out of the page [65].

orientated such that the z direction is along the neutrino beam line with the cathode to the left of the beam and the anode to the right. The active volume is defined as the volume enclosed by the LArTPC field cage which has a liquid argon mass of 90 tonnes out of a total 170 tonnes. The APA consists of three wire planes with the wires on the two induction planes orientated at $\pm 60^\circ$ to the vertical and the wires of the collection plane orientated vertically. Both the wire plane spacing and the wire pitch of each plane is 3 mm. Unlike SBND and ICARUS, the nominal electric field in MicroBooNE is 273 V/cm. The light collection system consists of a series of 32 PMTs and 4 lightguide paddles which are located directly behind the anode planes. The lightguides have a large collection area and their purpose is to guide light to the PMTs (the lightguide paddles were disfavoured once the ARAPUCA technology was developed.) [65].

MicroBooNE is also considered a surface level detector being only ~ 6 m underground and as there is no overburden present, a large flux of cosmic rays are observed. A CRT system similar to the one described in Section 2.5 for SBND was implemented. The CRT

system consists of 73 scintillating modules, however it is only sensitive to the four sides of the X and Y coordinates of the detector [62].

2.7. ICARUS

The ICARUS detector was first operated in 2010 and located at the Gran Sasso National Laboratory in Italy where it was used to detect events from cosmic rays and from the neutrino beam which is directed from CERN to Gran Sasso. In 2013 the decommissioning process began and the detector was taken to CERN for refurbishment before making its way to Fermilab and becoming part of the SBN program [55].

The ICARUS detector consists of two *modules* within a single cryostat with each module containing two TPCs. A schematic of this design is shown in Figure 2.13. Similar to SBND, the two TPCs within each module share a common cathode. The dimensions of each module are (3.6, 3.9, 19.6) m and the cryostat contains 760 tonnes of liquid argon with an active volume of 476 tonnes. Again, the APAs consists of three wire planes with a wire plane spacing and wire pitch of 3 mm. In contrast to SBND and MicroBooNE however, the wire planes are orientated at 0° for the first induction plane and at ±60° for the second induction plane and the collection plane. The choice of having a horizontal wire plane is due to ICARUS being initially designed to detect cosmic rays which would predominantly enter the detector from above and therefore be travelling perpendicular to the horizontal. The nominal electric field in each of the TPCs is 500 V/m [55].

The light collection system for ICARUS is comprised of a series of 74 PMTs positioned behind the wire planes. The layout of the PMTs is however asymmetric with the east module having a 3×9 array of PMTs for each TPC whereas the two TPCs in the west module have a single row of 9 PMTs plus two additional PMTs located centrally above and below the main row in the right chamber. Since the light is again produced with wavelengths in the VUV region, the PMTs are coated with TPB in order to shift the wavelength into the visible region [55].

The ICARUS CRT system surrounds the detector on all sides however the actual position is not always the same due to design choices. The CRT on the top most side

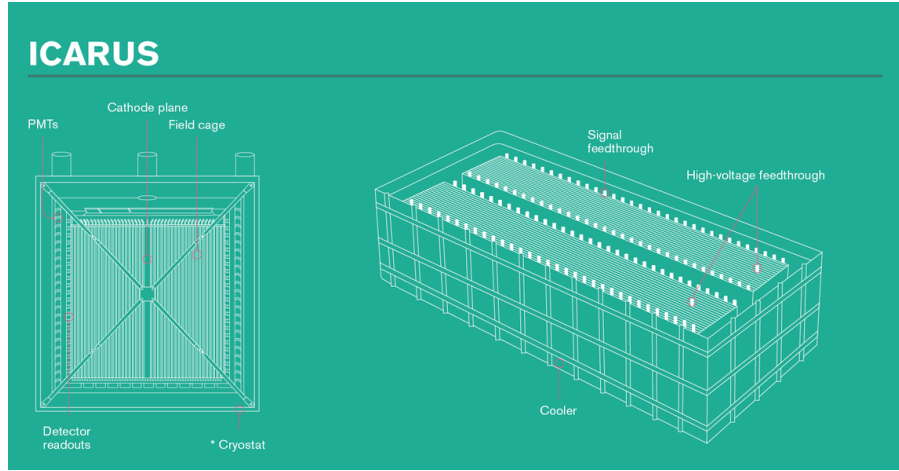


Figure 2.13.: Schematic of the ICARUS detector. The left image shows a cross-section of one of the two modules whereas the right image shows the whole detector with the two modules side by side [66].

which experiences the highest flux of cosmic rays, is located outside the TPC, about 3m from the top face above the readout electronics. It consists of two planes of scintillating modules with the readout coming from the same electronics board as is used by SBND. The CRT for the vertical sides are again outside the TPC and behind the PMT arrays and close to the cryostat walls. The scintillator modules from the MINOS experiment are being reused for this purpose. The CRT for the bottom face are the repurposed spare modules from the veto shield from the Double Chooz experiment and are located within the cryostat. Only about 50% of the bottom face is covered by the CRT because of limited space due to the supporting structure of the cryostat [55] [67].

2.8. SBN Physics Capabilities

The SBN program was designed with the aim of resolving the contentious results observed by a number of experiments as was discussed in Section 1.3. Since it was purposely planned with this in mind, the SBN program has a number of advantages over previous experiments in the hopes of detecting eV scale sterile neutrinos: it has a multi detector design, the near and far detector are positioned such that the oscillation signal is close to maximal for an

expected set of oscillation parameters, the detectors use the same technology and have the same target medium [42].

The top two plots of Figure 2.14 show the expected oscillation probability for the ν_e appearance channel as a function of the baseline for two sets of oscillation parameters, $(\sin^2 2\theta_{\mu e}, \Delta m_{41}^2) = (0.015, 0.3 \text{ eV}^2), (0.002, 1.5 \text{ eV}^2)$ and a neutrino energy of 700 MeV. The neutrino energy corresponds to the peak energy of the BNB and the oscillation points are chosen as the upper and lower limits of the global ν_e appearance data. In both cases there is a clear difference in the oscillation probability between the near and far detector showing that the SBN program is sensitive to oscillations within this parameter range [42]. The bottom two plots show the oscillation probability for the same two oscillation points as a function of neutrino energy for baselines of 110 m and 600 m. The ratio of the oscillation probability at 600 m to that at 110 m is also shown. Again there is a clear difference in the oscillation probability for most energies showing that the SBN program is sensitive to a wide range of neutrino energies [42]. The ν_e appearance oscillation sensitivity constructed at the time of the proposal is shown in Figure 2.15. These contours include the relevant backgrounds and systematic uncertainties with the exception of detector systematics.

The event rates in the near and far detector are correlated since both use the same interaction medium and the same technology to detect interactions. As Figure 2.14 shows, SBND will observe no or very few oscillated events and will give a measure of the absolute flux and interaction cross-section whereas both MicroBooNE and ICARUS are able to detect oscillated events with significant probability. Typically the BNB flux uncertainties and interaction cross-section uncertainties are fairly large, however, comparing results from SBND to MicroBooNE and ICARUS and noting the correlation between the detectors allows the uncertainties to be constrained [42].

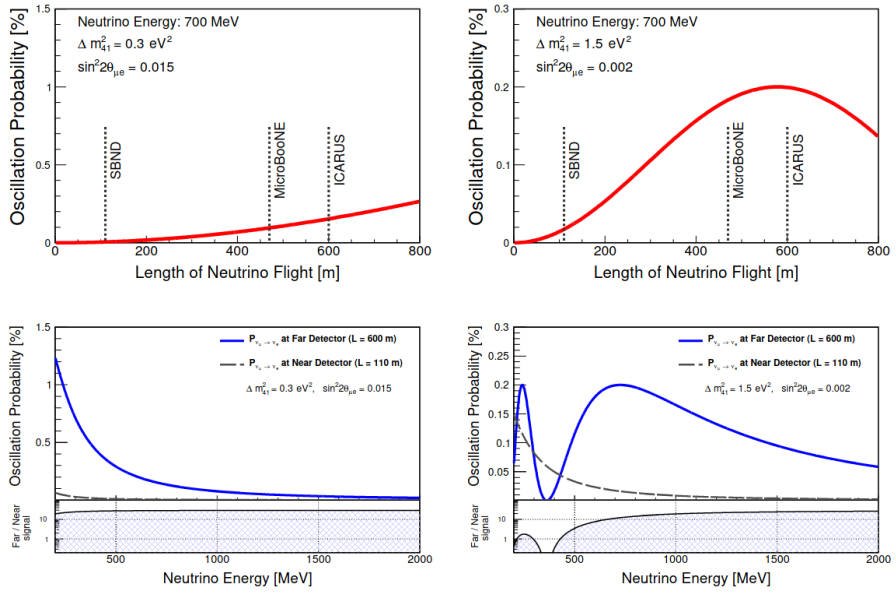


Figure 2.14.: The oscillation parameters used in the two left and right plots are $(\sin^2 2\theta_{\mu e}, \Delta m_{41}^2) = (0.015, 0.3 \text{ eV}^2), (0.002, 1.5 \text{ eV}^2)$ respectively. Top: The oscillation probability as a function of the baseline for the ν_e appearance channel. A neutrino energy of 700 MeV is used in both cases. Bottom: The oscillation probability is shown as a function of neutrino energy in both the near and far detector. Additionally, the ratio of the oscillation probabilities between the two detectors is also shown. [42]

This main goal of the SBN program revolves around sterile neutrino oscillation analyses, however the close proximity of the SBN detectors and in particular SBND to the neutrino beam source will allow for a high statistics study of neutrino argon interactions. This will provide valuable information for future liquid argon based experiments such as DUNE. SBND is expected to observe on the order of 2 million neutrino interactions a year which is sufficient to be able to minimise the associated uncertainty to a point such that systematic uncertainties become dominant. As the BNB consists predominantly of ν_μ , most events will also be ν_μ based, however the ν_e fraction of the BNB is sufficient to expect 12,000 ν_e events a year in SBND which is enough to perform both inclusive and exclusive analyses. There is also the opportunity to measure rare channels with a big increases in statistics or possibly even for the first time such as final states involving hyperons or $\nu_e \rightarrow \nu_e$ elastic scattering [42] [68].

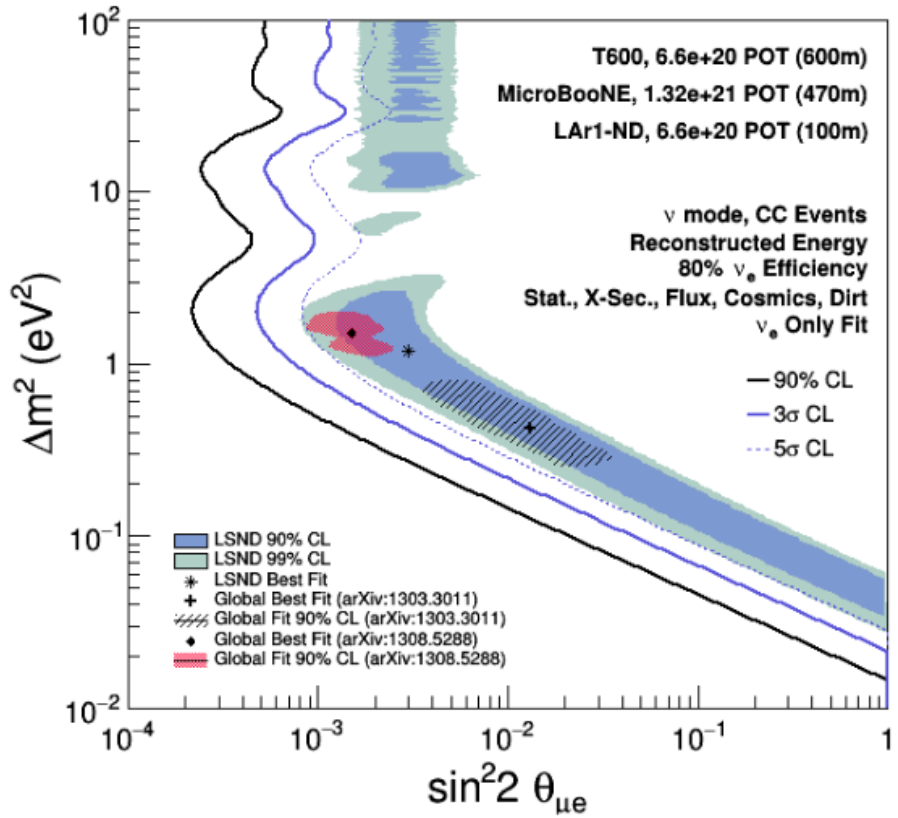


Figure 2.15.: The expected ν_e appearance sensitivity from the SBN program using inputs constructed at the time of the SBN proposal. Limits from LSND and global best fit results are also shown [55].

The large event rate and the high resolution event reconstruction provided may allow the SBN program to be sensitive to Beyond Standard Model (BSM) physics other than sterile neutrino oscillations [42]. The potential areas include, but are not limited to,

- Light Dark Matter - Assuming a dark matter particle has an associated light mediator particle which interacts with quarks, the high intensity proton beam will produce a dark matter beam alongside neutrinos. The dark matter particles will propagate to the detectors alongside the neutrinos where they may scatter off the argon nuclei. Neutrinos will however represent a large background in such search [42].
- Large Extra Dimensions - The neutrino mass scale could be explained by the presence of additional dimensions. The right handed neutrinos would be able to propagate in

the extra dimensions whilst the active neutrinos would be confined to the standard dimensions [42].

- Heavy Sterile Neutrinos - If heavy sterile neutrinos such as those present in the seesaw-mechanism discussed in Section 1.4.1 are of an MeV mass scale, they may be produced in the BNB via meson decay. They would then propagate along the beam line and their decay products may be observed in the detectors [42] [69].
- Dark Neutrinos - A beam neutrino interacts with an argon nucleus and scatters to a dark neutrino. The dark neutrino decays to a dark boson (and neutrino) and in turn the dark boson decays to an $e^+ e^-$ pair. This mechanism could provide an explanation to the MiniBooNE low energy excess [42] [70].

Chapter 3.

Sterile Neutrino Oscillation Inputs Within SBN

In order to perform an oscillation analysis, a number of inputs and analysis choices are required. Typically this involves generating some event sample in each detector for a given analysis, applying a physics hypothesis and some set of systematic uncertainties. A fit comparing the observed and predicted event rate is then performed giving the confidence level of the applied physics hypothesis. This is summarised in Figure 3.1 which shows the generic overview of the procedure coupled with the different components. Many of these items are common to all oscillation analyses and are agnostic to the fitting framework. The remainder of this chapter highlights some of the key inputs to the oscillation analysis along with some of the decisions that were made. The actual analysis results are detailed in Section ?? in addition to explaining how the VALEncia-Oxford-Rutherford (VALOR) framework processes or consumes these inputs where appropriate.

3.1. Event Production

The events used in this oscillation analysis are truth based with a *pseudo reconstruction* applied. Work on the reconstruction is still in progress and at the time of writing hasn't been sufficiently completed for it to be possible to generate a fully reconstructed event sample. The pseudo reconstruction involves applying energy smearing and a series of cuts

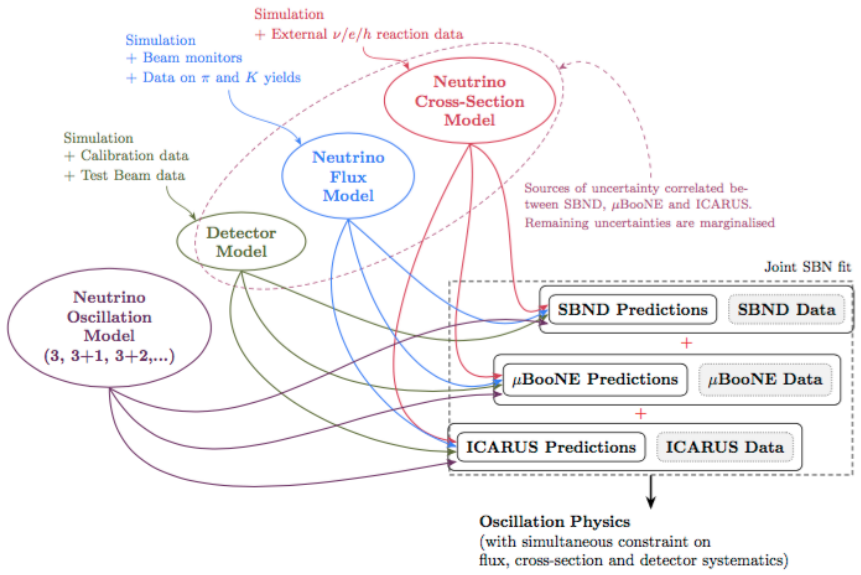


Figure 3.1.: Overview of the SBN oscillation analysis paradigm. A given model for the neutrino oscillation, detector, neutrino flux and neutrino cross-section are combined with the appropriate data to give the prediction for the respective detector. Individual detector predictions may be combined to give an overall SBN prediction.

to try and emulate a fully reconstructed sample. The details of the cuts that were applied to each of the analyses are discussed in Section 3.2.

Both the events for the ν_μ and ν_e sample were generated using Generates Events for Neutrino Interaction Experiments (GENIE)v3 (specifically the G1810a0211a tune) and then propagated through GEometry ANd Tracking (GEANT4) using the Liquid Argon Software (LArSoft) framework [71] [72] [73]. For the ν_μ sample, this involved generating $\sim 1,000,000$ intrinsic ν_μ events in each detector. The ν_e sample is a little more involved since in addition to generating an intrinsic sample, an oscillated $\nu_\mu \rightarrow \nu_e$ sample, a dirt sample and a cosmic sample also needed to be produced. The oscillated sample is used to mimic the ν_e appearance signal whereas the dirt and cosmic samples are backgrounds. The other major background associated with a ν_e analysis involves ν_μ . A dedicated sample was not produced to emulate this, but instead, the events from the ν_μ production were also run through the ν_e selection. Table 3.1 outlines the number of events produced for the ν_e sample for each sub-sample for each detector. The dirt events were produced with an additional filter at the generation stage which discarded any events where a shower above

10 MeV in the active volume was not present. This filter was used in order to remove any delta rays. Only about 1% of dirt events would pass this filter so the number of dirt events used in the ν_e selection was $\sim 100,000$.

Sample	Events Produced
Intrinsic ν_e	$\sim 1,000,000$
Oscillated ν	$\sim 1,000,000$
ν_μ	Used ν_μ sample
Dirt	$\sim 10,000,000$
Cosmic	$\sim 100,000$

Table 3.1.: The number of events initially produced for each sample in each of the three SBN detectors as part of the ν_e analysis.

The actual number of real ν_μ events expected in SBND is well over 5 million for about 3 years of data taking [74]. Generating this many events isn't feasible as part of a Monte Carlo (MC) production, hence the above number of events were generated. The MC events produced have an associated Protons-On-Target (POT) so the number of events may be scaled to the nominal POT of each experiment. For SBND and ICARUS the nominal POT is 6.6×10^{20} which corresponds to around 3 years of data taking. Since MicroBooNE has already been collecting data for some time, the nominal POT is 1.32×10^{21} . Due to scaling the generated event rate to the nominal POT this results in non-integer number of events as is seen for example in Table ??.

3.2. Event Selection

[Link in with Energy Reco. section](#)

The event selections are performed in order to first identify ν_μ or ν_e -like interactions. The selection steps for each of the analyses are outlined below and are performed for each associated event.

3.2.1. ν_μ Selection

1. Remove any events whose true interaction vertex is not located in the fiducial volume.
2. If no muon or charged pion track are produced, remove the event. A muon corresponds to a CC signal event whereas a charged pion is possibly due to NC background events.
3. If the primary track has a true kinetic energy less than 21 MeV, remove the event.
4. If the primary track has a length less than 50 cm and is fully contained in the detector, remove the event.
5. If the primary track exits the detector and has a length less than 100 cm, remove the event.
6. A weight of 0.8 is applied to all selected events to account for an assumed 80% reconstruction efficiency [75].

3.2.2. ν_e Selection

The ν_e selection follows a similar basis to the ν_μ selection described in section 3.2.1, however different criteria for the selection were applied to beam induced TPC events, dirt events and cosmic events, each of which are outlined below.

Beam induced active volume events

1. Remove any events whose true interaction vertex is not located in the fiducial volume.
2. Showers arising from the vertex are identified and the reconstructed energy is found from smearing the ionisation deposition. If more than one shower with energy above 100 MeV exists, the event is removed. This removes neutral pion events where the pion decays into two photon showers.
3. If there is only one photon candidate in the event, a conversion gap cut is applied. If the vertex is deemed visible, due to the presence of at least 50 MeV of hadronic

kinetic energy, and the photon starts to shower further than 3 cm from the vertex the event is removed.

4. Remaining photons undergo a dE/dx cut resulting in a 94% background rejection.
5. If a misidentified photon originates from a resonant ν_μ CC interaction, the muon lepton is identified. Events where a muon travels greater than 1 m are assumed to be from ν_μ CC interactions and the event is removed.
6. Events where the shower has an energy less than 200 MeV are removed.
7. A weight of 0.8 is applied to all selected events to account for an assumed 80% reconstruction efficiency [76].

Dirt Events

The selection procedure for dirt events is similar to that of events occurring in the TPC outlined above. However, since the vertex for dirt events occurs outside the detector volume, the conversion gap and muon track length cuts are not undertaken [76].

Cosmic Events

A largely separate analysis is applied for cosmic events which is as follows:

1. If a cosmic photon initially interacts outside the fiducial volume the event is removed.
2. Cosmic events which occur outside the beam spill time window are removed if there is no other activity in the TPC during the beam spill time.
3. 95% of cosmic events occurring within the beam spill window are removed by use of the PDS and CRT systems and taking advantage of the bucket structure of the beam.
4. Same dE/dx cut as described above.
5. Events below a reconstructed energy of 200 MeV are removed.

6. A topological cosmic cylinder cut is applied to cosmic photons which originate from cosmic muons that pass through the TPC. These can be removed by a fiducial volume cut corresponding to a cylinder of radius 15 cm around the cosmic muon [76].

3.3. Reaction Modes

The reaction modes define the type of neutrino-nucleus interaction. They are categorised in terms of two sets: The *fine* reaction modes outline the complete list of all possible reaction modes whereas the *coarse* reaction modes define a broader class of interaction which encompass one or more fine reaction mode. The fine reaction modes are listed in Table 3.2 and are typically used at the analysis level. The coarse reaction modes used depend on the analysis channel and are listed in Table 3.3. They are usually only used when displaying data such as in a breakdown of event rate spectra since using the complete list of reaction modes would be impractical.

Fine Reaction Modes

$\nu_\mu, \bar{\nu}_\mu$	$\nu_e, \bar{\nu}_e$	$\nu_\mu \rightarrow \nu_e, \bar{\nu}_\mu \rightarrow \bar{\nu}_e$
CC QE	CC QE	CC QE
NC Elastic	NC Elastic	CC MEC
CC, NC MEC	CC, NC MEC	CC $1\pi^\pm$
CC, NC $1\pi^\pm$	CC, NC $1\pi^\pm$	CC $1\pi^0$
CC, NC $1\pi^0$	CC, NC $1\pi^0$	CC $2\pi^\pm$
CC, NC $2\pi^\pm$	CC, NC $2\pi^\pm$	CC $2\pi^0$
CC, NC $2\pi^0$	CC, NC $2\pi^0$	CC Coh
CC, NC $\pi^\pm \pi^0$	CC, NC $\pi^\pm \pi^0$	Elastic Scattering
CC, NC Coh	CC, NC Coh	CC Other
CC, NC Elastic Scattering	CC+NC Elastic Scattering	
NC 1γ	NC 1γ	
CC, NC Other	CC, NC Other	

Cosmic & Dirt

Table 3.2.: The complete list of reaction modes considered in an SBN analysis.

<i>Coarse Reaction Modes</i>	
$\nu_\mu, \bar{\nu}_\mu$	$\nu_e, \bar{\nu}_e$
ν_μ CC QE	ν_e CC QE
ν_μ CC MEC	ν_e CC MEC
ν_μ CC 1π	ν_e CC 1π
ν_μ CC 2π	ν_e CC 2π
ν_μ CC Other	ν_e CC Other
$\bar{\nu}_\mu$ CC	$\bar{\nu}_e$ CC
ν_e & $\bar{\nu}_e$ CC	ν_μ CC
NC	$\bar{\nu}_\mu$ CC
<i>Cosmic</i>	Oscillated ν_e CC
<i>Dirt</i>	NC 0π
	NC Other
	<i>Cosmic</i>
	<i>Dirt</i>

Table 3.3.: The *coarse* reaction modes used for both the ν_μ and ν_e channels. These are a broader definition of the reaction modes where one or more of the *fine* reaction modes listed in Table 3.2 would come under the umbrella of a given coarse reaction mode.

3.4. Systematic Uncertainties

The majority of flux and interaction systematics considered are provided by the MicroBooNE and GENIE reweight schemes respectively [54] [77]. The two exceptions are the POT normalisation and MEC uncertainty which are handled separately as described below. For each MC event, both reweight packages generate N associated *universes* where the given parameters are randomly varied within their limits. This allows changes in event rate spectra to be related to systematic parameter variations. The systematic parameters considered are described below along with a table quoting their estimated uncertainty.

3.4.1. Flux Systematics

The flux systematics are generally all grouped together, however, there are 3 distinct sets with different origins as part of the MiniBooNE reweight scheme which are detailed below plus the additional POT normalisation.

Optical Flux Systematics

The optical flux systematics are comprised of two parameters; the *skin effect* and the *horn current*. The horn current parameter is simply the uncertainty of the supplied current to the focusing horn. Since the current is linked to the focusing properties of the horn, uncertainty on the current leads to an uncertainty on the neutrino flux. The focusing horn is surrounded by a conductor where currents travel on the surface of the conductor. The skin effect is a measure of how much these surface currents penetrate into the conductor which in turn affects the internal fields of the conductor. Therefore, due to the skin effect, the strength of the magnetic field that particles propagating through the horn experience may vary [54].

Parameter	Description	Uncertainty
$f_{SkinEffect}$	Depth that the current penetrates the horn conductor	< 18%
$f_{HornCurrent}$	Current running in the horn conductor	$\pm 0.6\%$

Table 3.4.: Optical systematic flux uncertainties associated with the current in the horn [54].

Secondary Hadron Interaction Cross-Sections

The proton interaction rate in BNB target is largely dependent on the hadronic cross-sections with the beryllium target and aluminium horn. These cross-sections are divided into three categories; elastic scattering, quasi-elastic scattering and inelastic scattering. The total cross-section, σ_{TOT} , is defined as the sum of the elastic, σ_{EL} and inelastic, σ_{INEL} , cross-sections. The quasi-elastic cross-section, σ_{QE} , is a subset of the σ_{INEL} cross-section. The σ_{TOT} variations are based on comparing calculations with neutron-nucleus measurements. The model describing σ_{TOT} is assumed to work sufficiently well for π^\pm -nucleus interactions and is extended to include these interactions in addition to all nucleon-nucleus interactions. σ_{INEL} is estimated directly from the available data and the deviations are therefore noticeably smaller than for σ_{TOT} . The variations are chosen to encompass the uncertainties in the measurements. σ_{QEL} variations are again estimated from a combination of the available data and models. Finally, the linked relationship between the different cross-section is considered such that: 1) If σ_{INEL} is fixed, a variation in σ_{TOT} will result in a variation in σ_{EL} . 2) If σ_{INEL} is varied, the relative contribution from σ_{INEL} and σ_{EL} to σ_{TOT} (which remains constant) will vary. 3) If σ_{QEL} is varied, the relative contribution from other inelastic process to σ_{INEL} (which remains constant) will vary [54].

The above approach is applied for both beryllium and aluminium nuclei and the uncertainty associated with the total, quasi-elastic and inelastic cross-sections for both nucleons and pions for the two nuclei are shown in Table 3.5.

Parameter	Description	Uncertainty	
		Be	Al
$f_{\sigma_{INEL}^N}$	Secondary inelastic nucleon cross-section in the target (Be) and horn (Al)	$\pm 5\%$	$\pm 10\%$
$f_{\sigma_{QE}^N}$	Secondary quasi-elastic nucleon cross-section in the target (Be) and horn (Al)	$\pm 20\%$	$\pm 45\%$
$f_{\sigma_{TOT}^N}$	Secondary total nucleon cross-section in the target (Be) and horn (Al)	$\pm 15\%$	$\pm 25\%$
$f_{\sigma_{INEL}^\pi}$	Secondary inelastic pion cross-section in the target (Be) and horn (Al)	$\pm 10\%$	$\pm 20\%$
$f_{\sigma_{QE}^\pi}$	Secondary quasi-elastic pion cross-section in the target (Be) and horn (Al)	$\pm 11.2\%$	$\pm 25.9\%$
$f_{\sigma_{TOT}^\pi}$	Secondary total pion cross-section in the target (Be) and horn (Al)	$\pm 11.9\%$	$\pm 28.7\%$

Table 3.5.: The systematic uncertainties associated with secondary hadron interaction cross-sections in both the horn (Aluminium) and the target (Beryllium) [55]

Hadronic Neutrino Production Flux Uncertainties

The majority of neutrinos in the BNB are due to decaying particles which are a result of protons interacting with the beryllium target. Understanding the neutrino flux, therefore, relies on understanding the production of the particles decaying to neutrinos, which are predominately pions for ν_μ and kaons for ν_e (plus the decay of muons which in turn are produced in the meson decays).

The Sanford-Wang parameterisation is used to estimate the π^\pm production. It depends on the meson momentum, p , and angle relative to the incident proton, θ , and also the proton momentum, p_B . The parametrisation is given by

$$\frac{d^2\sigma}{dpd\theta} = c_1 p^{c_2} \left(1 - \frac{p}{p_B - c_9}\right) \exp\left(-c_3 \frac{p^{c_4}}{p_B^{c_5}} - c_6 \theta(p - p_B c_7 \cos^{c_8} \theta)\right), \quad (3.1)$$

where parameters $c_{1 \rightarrow 9}$ are determined from the HARP (8.89 GeV/c), BNL E910 (6.4 GeV/c) and BNL E910 (12.3 GeV/c) experiments [54].

No k^+ production rates exist for proton-beryllium interactions at 8.89 GeV/c which is the primary BNB operating momentum. To estimate the k^+ production rate at the BNB momentum, Feynman scaling is used to extrapolate the rate from production rates at nearby energies [54].

The major contribution that the k^0 makes to the BNB flux is from the decay of the k_L^0 . The k^0 that are produced via strong interactions have equal contents of k_L^0 and k_s^0 , therefore the production rate of k_L^0 can be inferred from knowing the production rate of k_s^0 . The Sanford-Wang parametrisation is again used to estimate the production cross-section by combining data from the BNL E910 experiment at 12.3 GeV/c and 17.5 GeV/c and the KEK experiment at 12.3 GeV/c.

For the k^- , there is minimal production data available, therefore, simulations are used exclusively. The rate and spectrum of the k^- are estimated by simulating 8.89 GeV/c proton-beryllium interactions [54].

Parameter	Description	Uncertainty			
		ν_μ	$\bar{\nu}_\mu$	ν_e	$\bar{\nu}_e$
f_{π^+}	ν production mechanism: π^+	$\pm 11.7\%$	$\pm 1.0\%$	$\pm 10.7\%$	$\pm 0.03\%$
f_{π^-}	ν production mechanism: π^-	$\pm 0.0\%$	$\pm 11.6\%$	$\pm 0.0\%$	$\pm 3.0\%$
f_{K^+}	ν production mechanism: K^+	$\pm 0.2\%$	$\pm 0.1\%$	$\pm 2.0\%$	$\pm 0.1\%$
f_{K^-}	ν production mechanism: K^-	$\pm 0.0\%$	$\pm 0.4\%$	$\pm 0.0\%$	$\pm 3.0\%$
f_{K^0}	ν production mechanism: K^0	$\pm 0.0\%$	$\pm 0.3\%$	$\pm 2.3\%$	$\pm 21.4\%$

Table 3.6.: Hadronic neutrino production systematic flux uncertainties [78].

BNB POT Normalisation

The intensity of the proton beam is monitored by two toroids and it has been found that the two toroids agree with one another to within 2% [54]. An additional 2% normalisation

uncertainty is applied in order to account for this POT accounting uncertainty. This uncertainty is set so that it is fully correlated between all analysis bins.

3.4.2. Interaction Systematics

The uncertainties associated with neutrino interactions are provided by GENIE and are implemented using the GENIE ReWeight package. This is the case for all the interaction systematics considered here except for the MEC systematic (see Section 3.4.2). The GENIE reweighting scheme works as follows: For each quantity, P , which has an associated uncertainty, a systematic parameter, x_P is introduced. Varying x_P will modify, P such that

$$P \rightarrow P' = P(1 + x_P \cdot \frac{\delta P}{P}), \quad (3.2)$$

where δP represents the standard deviation of P . It follows from Equation 3.2 that for a $x_P = 0$, $P' = P$ and for $x_P = \pm 1$, $P' = P \pm \delta P$.

The two main types of interaction systematics considered in this analysis are cross-section and intranuclear hadron transport model uncertainties, however, within an SBN analysis, the interaction systematics are generally grouped into two categories: the *proposal* and *modern* set of parameters. The proposal systematics are those that were included as part of the analysis done at the time of the SBN proposal, whereas the modern systematics represent the additional systematics which have been deemed relevant for SBN in the period following the proposal [55]. The details of how GENIE handles cross-section and intranuclear hadron transport parameters is detailed below, followed by outlining which parameters are included as part of the proposal and modern set of parameters.

Neutrino Cross-Section uncertainties

The neutrino cross-section gives a measure of the neutrino interaction probability. The event weight, w_σ^{evt} , associated with a given parameter for a neutrino cross-section is

calculated via

$$w_\sigma^{evt} = \left(\frac{d^n \sigma'_\nu}{dK^n} \right) \Bigg/ \left(\frac{d^n \sigma_\nu}{dK^n} \right), \quad (3.3)$$

where $\frac{d^n \sigma'_\nu}{dK^n}$ is the differential cross-section with varied physics parameters and $\frac{d^n \sigma_\nu}{dK^n}$ is the nominal differential cross-section with K^n being the kinematical phase space in both cases [77].

Intranuclear hadron transport uncertainties

When hadrons are produced in the nucleus they may interact as they propagate out of the nucleus. The reinteraction in the nucleus may significantly alter the observed final state particles. There are two primary uncertainties considered with this effect: The uncertainty in the overall probability of rescattering and the uncertainty corresponding to the probability of each rescattering mode once it has been determined that rescattering will occur for a given hadron [77].

For a hadron propagating in the nucleus, the survival probability, P_{surv}^h , is calculated as

$$P_{surv}^h = \int e^{-r/\lambda^h(\vec{r}, h, E_h)} dr, \quad (3.4)$$

where the integral is evaluated along the hadron path and λ^h is the mean free path. The probability of rescattering, P_{rescat}^h , is then defined as

$$P_{rescat}^h = 1 - P_{surv}^h. \quad (3.5)$$

The mean free path is a function of the hadron type, h , the hadron energy, E_h and position, \vec{r} and is given by

$$\lambda^h = \frac{1}{\rho_{nucl}(r) \cdot \sigma^{hN}(E_h)}, \quad (3.6)$$

where $\rho_{nucl}(r)$ is the density profile of the nucleus and $\sigma^{hN}(E_h)$ is the total cross-section of the hadron-nucleon [77].

In terms of reweighting, for a given systematic parameter, x_{mfp}^h , with an uncertainty, $\delta\lambda^h$, the mean free path may be tweaked such that

$$\lambda^h \rightarrow \lambda^{h'} = \lambda^h \left(1 + x_{mfp}^h \frac{\delta\lambda^h}{\lambda^h} \right), \quad (3.7)$$

where $\lambda^{h'}$ is the tweaked mean free path. The modified survival probability, $P_{surv}^{h'}$, is then found by substituting $\lambda^{h'}$ into Equation 3.4. The weight, w_{mfp}^h , associated with a given change in the mean free path is calculated as [77]

$$w_{mfp}^h = \begin{cases} \frac{1-P_{surv}^{h'}}{1-P_{surv}^h}, & \text{if } h \text{ reinteracts} \\ \frac{P_{surv}^{h'}}{P_{surv}^h}, & \text{if } h \text{ escapes.} \end{cases} \quad (3.8)$$

Once it has been determined that a hadron will rescatter, the following scattering modes are considered: elastic, inelastic, charge exchange, absorption and pion production. The probability of a given mode, P_f^h , occurring is given by

$$P_f^h = \frac{\sigma_f^{hA}}{\sigma_{total}^{hA}}, \quad (3.9)$$

where σ_f^{hA} is the cross-section for the given hadron-nucleus mode and σ_{total}^{hA} is the total hadron-nucleus cross-section. Similarly to the mean free path, the hadron-nucleus cross-section of a mode may be tweaked such that

$$\sigma_f^{hA} \rightarrow \sigma_f^{hA'} = \sigma_f^{hA} \left(1 + x_f^h \frac{\delta\sigma_f^{hA}}{\sigma_f^{hA}} \right), \quad (3.10)$$

where $\sigma_f^{hA'}$ is the tweaked cross-section, x_f^h is a systematic parameter and $\delta\sigma_f^{hA}$ is the associated uncertainty. The weight of a mode, w_{mode}^h , is given by

$$w_{mode}^h = \sum_f \delta_{ff'} \cdot x_f^h \cdot \frac{\delta\sigma_f^{hA}}{\sigma_f^{hA}}, \quad (3.11)$$

where the sum is over the possible rescattering modes, f' is the actual mode for the given hadron, and $\delta_{ff'}$ is the Kronecker delta between f and f' [77].

The total weight of a single hadron, w^h , is then given by the product of the two weights such that,

$$w^h = w_{mfp}^h \cdot w_{mode}^h. \quad (3.12)$$

For a single neutrino event, there may be multiple hadrons present, therefore the total weight, w_{HT}^{evt} , for a neutrino event is given by the product of individual hadron weights,

$$w_{HT}^{evt} = \prod_j w_j^h, \quad (3.13)$$

where the index j corresponds to all the primary hadrons [77].

Proposal Interaction Systematics

The proposal systematics only included a set of cross-section parameters which are listed in Table 3.7 along with their uncertainty.

Parameter	Description	$\delta P/P$
$f_{M_A^{CCQE}}$	Axial mass for CC quasi-elastic	-15% +25%
$f_{M_A^{CCRes}}$	Axial mass for CC resonance neutrino production	$\pm 20\%$
$f_{M_A^{NCRes}}$	Axial mass for NC resonance neutrino production	$\pm 20\%$
f_{NC}	Additional error on NC/CC ratio	$\pm 25\%$
$f_{nR_{\nu n}^{CC1\pi}}$	Non-resonance bkg normalisation in νn CC1 π reactions	$\pm 50\%$
$f_{nR_{\nu p}^{CC1\pi}}$	Non-resonance bkg normalisation in νp CC1 π reactions	$\pm 50\%$
$f_{nR_{\nu n}^{CC2\pi}}$	Non-resonance bkg normalisation in νn CC2 π reactions	$\pm 50\%$
$f_{nR_{\nu p}^{CC2\pi}}$	Non-resonance bkg normalisation in νp CC2 π reactions	$\pm 50\%$
$f_{nR_{\bar{\nu} n}^{CC1\pi}}$	Non-resonance bkg normalisation in $\bar{\nu} n$ CC1 π reactions	$\pm 50\%$
$f_{nR_{\bar{\nu} p}^{CC1\pi}}$	Non-resonance bkg normalisation in $\bar{\nu} p$ CC1 π reactions	$\pm 50\%$
$f_{nR_{\bar{\nu} n}^{CC2\pi}}$	Non-resonance bkg normalisation in $\bar{\nu} n$ CC2 π reactions	$\pm 50\%$
$f_{nR_{\bar{\nu} p}^{CC2\pi}}$	Non-resonance bkg normalisation in $\bar{\nu} p$ CC2 π reactions	$\pm 50\%$
$f_{nR_{\nu n}^{NC1\pi}}$	Non-resonance bkg normalisation in νn NC1 π reactions	$\pm 50\%$
$f_{nR_{\nu p}^{NC1\pi}}$	Non-resonance bkg normalisation in νp NC1 π reactions	$\pm 50\%$
$f_{nR_{\nu n}^{NC2\pi}}$	Non-resonance bkg normalisation in νn NC2 π reactions	$\pm 50\%$
$f_{nR_{\nu p}^{NC2\pi}}$	Non-resonance bkg normalisation in νp NC2 π reactions	$\pm 50\%$
$f_{nR_{\bar{\nu} n}^{NC1\pi}}$	Non-resonance bkg normalisation in $\bar{\nu} n$ NC1 π reactions	$\pm 50\%$
$f_{nR_{\bar{\nu} p}^{NC1\pi}}$	Non-resonance bkg normalisation in $\bar{\nu} p$ NC1 π reactions	$\pm 50\%$
$f_{nR_{\bar{\nu} n}^{NC2\pi}}$	Non-resonance bkg normalisation in $\bar{\nu} n$ NC2 π reactions	$\pm 50\%$
$f_{nR_{\bar{\nu} p}^{NC2\pi}}$	Non-resonance bkg normalisation in $\bar{\nu} p$ NC2 π reactions	$\pm 50\%$

Table 3.7.: GENIE interaction cross-section systematics considered in SBN as part of the proposal set of systematics. [77].

Modern Interaction Systematics

The modern systematics include an additional set of cross-section parameters which are listed in Table 3.8 in addition to a set of intranuclear hadron transport parameters which

are listed in Table 3.9. Again, both tables also show the associated uncertainty of each parameter. The MEC uncertainty mentioned is also considered as part of the modern systematic parameters and is detailed below.

Parameter	Description	$\delta P/P$
$f_{M_A^{NCEl}}$	Axial mass for NC elastic	$\pm 25\%$
$f_{\eta^{NCEl}}$	Strange axial form factor for NC elastic	$\pm 30\%$
$f_{M_V^{CCRes}}$	Vector mass for CC resonance neutrino production	$\pm 10\%$
$f_{M_V^{NCRes}}$	Vector mass for NC resonance neutrino production	$\pm 10\%$
$f_{A_{HT}}$	Higher-twist parameter A for NC and CC DIS events	$\pm 25\%$
$f_{B_{HT}}$	Higher-twist parameter B for NC and CC DIS events	$\pm 25\%$
$f_{C_{v1u}}$	Valence p.d.f. correction factor C_{v1u} for DIS events	$\pm 30\%$
$f_{C_{v2u}}$	Valence p.d.f. correction factor C_{v2u} for DIS events	$\pm 40\%$
$f_{M_A^{Coh}}$	Axial mass for NC and CC coherent pion production	$\pm 50\%$
$f_{R_0^{Coh}}$	Nuclear size parameter controlling π absorption	$\pm 20\%$
$f_{\Delta \rightarrow N\gamma}$	Branching ratio for Δ radiative decay	$\pm 50\%$

Table 3.8.: GENIE interaction cross-section systematics considered in SBN as part of the modern set of systematics [77].

Parameter	Description	$\delta P/P$
f_{λ_π}	Intranuclear mean free path for pions	$\pm 20\%$
$f_{R_\pi^{CEx}}$	Intranuclear charge exchange rescattering fraction for pions	$\pm 50\%$
$f_{R_\pi^{Inel}}$	Intranuclear inelastic rescattering fraction for pions	$\pm 40\%$
$f_{R_\pi^\pi}$	Intranuclear pion-production rescattering fraction for pions	$\pm 20\%$
$f_{R_\pi^{Abs}}$	Intranuclear absorption fraction for pions	$\pm 20\%$
f_{λ_N}	Intranuclear mean free path for nucleons	$\pm 20\%$
$f_{R_N^{CEx}}$	Intranuclear charge exchange rescattering fraction for nucleons	$\pm 50\%$
$f_{R_N^{Inel}}$	Intranuclear inelastic rescattering fraction for nucleons	$\pm 40\%$
$f_{R_N^\pi}$	Intranuclear pion-production rescattering fraction for nucleons	$\pm 20\%$
$f_{R_N^{Abs}}$	Intranuclear absorption fraction for nucleons	$\pm 20\%$

Table 3.9.: Intranuclear hadron transport systematic parameters considered in SBN as part of the modern set of systematics [77].

MEC uncertainty

A MEC uncertainty parameter which specifically affects MEC events is not included from the GENIE event generator since it was decided that the parameter was not sufficiently validated. Instead, a 100% normalisation uncertainty is applied to all MEC events. The value of the uncertainty was chosen to be a 100% (maximal) to ensure the effect of the MEC parameter would not be an underestimate.

3.4.3. Other Systematics

Efficiency systematics and energy scale systematics are not implemented in the *standard* analyses because there currently isn't a good handle on how to correctly quantify them. A rigorous scheme akin to those described in Section 3.4.1 and Section 3.4.2 doesn't exist, so instead in-house methods have been developed which are described below.

Efficiency Systematics

The current scheme for implementing efficiency (detector) systematics into a fit is by use of a covariance matrix where each element is defined by the systematics outlined in Table 3.10. This allows for the lack of associated event reweighting schemes to be bypassed whilst still being able to capture varying uncertainties being applied to different kinematic ranges, detectors and signal or background processes in each sample. In general, we assume that a covariance matrix \mathcal{M}_{ij} is comprised of both correlated and uncorrelated uncertainties such that

$$\mathcal{M}_{ij} = \mathcal{M}_{ij}^{corr} + \mathcal{M}_{ij}^{uncorr}, \quad (3.14)$$

where \mathcal{M}_{ij}^{corr} is the correlated component and $\mathcal{M}_{ij}^{uncorr}$ is the uncorrelated component. For correlated uncertainties,

$$\mathcal{M}_{ij}^{corr} = \begin{cases} \sigma_i^2, & i = j \\ C_{ij}\sigma_i\sigma_j, & i \neq j, \end{cases} \quad (3.15)$$

where C_{ij} represents the correlation between the off-diagonal elements and $\sigma_{i,j}$ is some percentage error associated with each systematic. In the case of fully correlated uncertainties, C_{ij} reduces to one and $\sigma_i = \sigma_j$. For uncorrelated uncertainties,

$$\mathcal{M}_{ij}^{uncorr} = \begin{cases} \sigma_i'^2, & i = j \\ 0, & i \neq j, \end{cases} \quad (3.16)$$

with σ'_i again being a percentage error. If any correlated errors are assumed to be fully correlated, \mathcal{M}_{ij} will then have diagonal elements given by $\sigma_i^2 + \sigma'_i{}^2$ and off diagonal elements given by σ_i^2 .

Applies to					
Systematic	Beam	Detector	Sample	Mode	Reco. energy bin edges
$f_0 - f_7$	FHC	SBND	ν_μ CC-like	signal/ ν_μ CC	{0, 0.2, 0.4, 0.6, 0.8, 1.0, 1.5, 2.0, ∞ }
$f_8 - f_{13}$	FHC	SBND	ν_μ CC-like	bkg/NC	{0, 0.2, 0.4, 0.6, 0.8, 1.0, ∞ }
f_{14}	FHC	SBND	ν_μ CC-like	bkg/Dirt	{0, ∞ }
f_{15}	FHC	SBND	ν_μ CC-like	bkg/Cosmics	{0, ∞ }
$f_{16} - f_{24}$	FHC	SBND	ν_e CC-like	signal/ ν_e CC	{0, 0.2, 0.4, 0.6, 0.8, 1.0, 1.5, 2.0, 3.0, ∞ }
$f_{25} - f_{33}$	FHC	SBND	ν_e CC-like	bkg/ ν_μ CC	{0, 0.2, 0.4, 0.6, 0.8, 1.0, 1.5, 2.0, 3.0, ∞ }
$f_{34} - f_{42}$	FHC	SBND	ν_e CC-like	bkg/NC1 γ	{0, 0.2, 0.4, 0.6, 0.8, 1.0, 1.5, 2.0, 3.0, ∞ }
$f_{43} - f_{51}$	FHC	SBND	ν_e CC-like	bkg/NC1 π^0	{0, 0.2, 0.4, 0.6, 0.8, 1.0, 1.5, 2.0, 3.0, ∞ }
$f_{52} - f_{60}$	FHC	SBND	ν_e CC-like	bkg/NCother	{0, 0.2, 0.4, 0.6, 0.8, 1.0, 1.5, 2.0, 3.0, ∞ }
$f_{61} - f_{66}$	FHC	SBND	ν_e CC-like	bkg/Dirt	{0, 0.2, 0.4, 0.6, 0.8, 1.0, ∞ }
$f_{67} - f_{72}$	FHC	SBND	ν_e CC-like	bkg/Cosmics	{0, 0.2, 0.4, 0.6, 0.8, 1.0, ∞ }
$f_{73} - f_{145}$	As above, but for μ B				
$f_{146} - f_{218}$	As above, but for ICARUS				

Table 3.10.: The binning scheme used to produce the efficiency uncertainty covariance matrices.

All future discussion involving correlated uncertainties should from here on be assumed to be fully correlated even if not explicitly stated. A set of example covariance matrices are shown in Figure 3.2. The top left plot corresponds to a 10% correlated error only. The remaining three plots all have a correlated error of 2%, with some varying amounts of an uncorrelated error associated with each systematic.

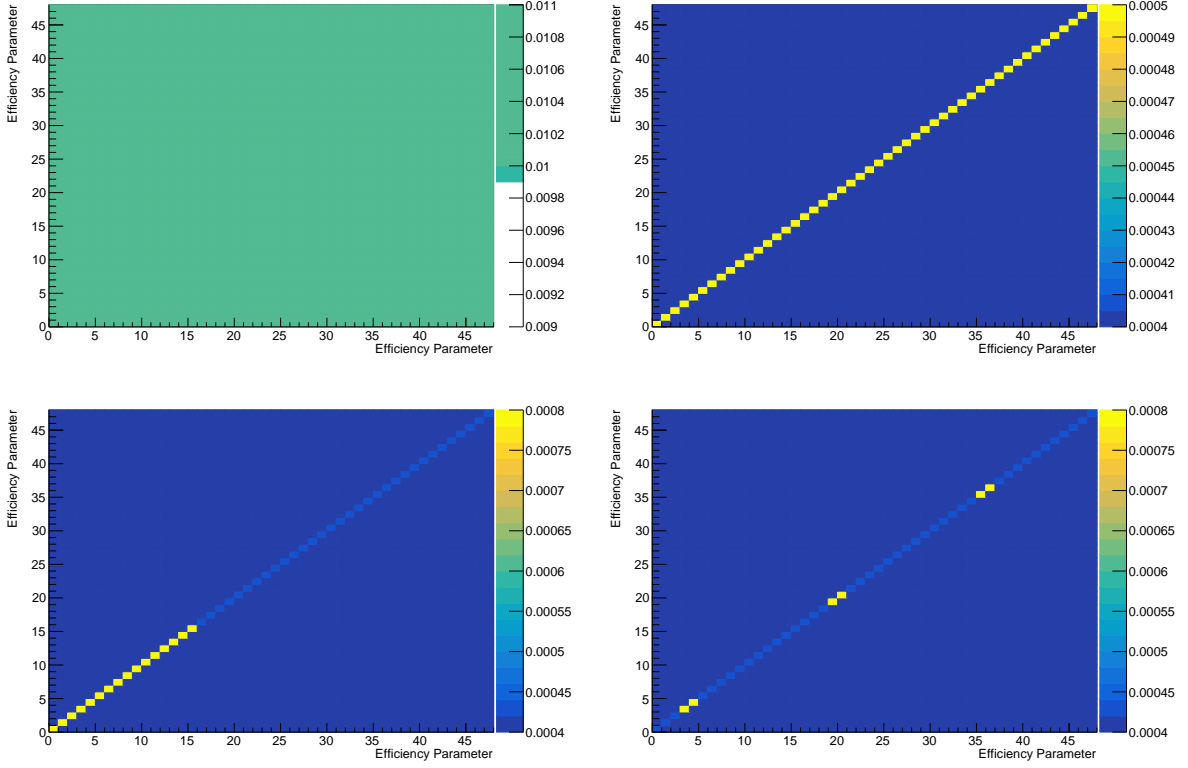


Figure 3.2.: Covariance matrices produced to investigate the effects of efficiency systematics for the ν_μ disappearance channel. Top left: A 10% fully correlated error only. Top right: A 2% fully correlated error with an additional 1% uncorrelated error across all bins. Bottom left: A 2% fully correlated error with an additional 2% uncorrelated error for all SBND bins and a 0.5% uncorrelated error for all MicroBooNE and ICARUS bins. Bottom right: A 2% fully correlated error with an additional 2% uncorrelated error for the peak energy bins (0.6 - 1.0 GeV) in each detector and a 0.5% uncorrelated error for all other bins.

Energy Scale Systematic

The energy scale systematic is a global systematic to account for the fact that events are binned based on their energy. Uncertainty on the reconstructed neutrino energy means that it's possible certain events to *migrate* between energy bins. Since the energy distribution of events isn't flat, this migration would in general not be uniform. If the neutrino energy were to be 'dialled-up', the number of events migrating from a given bin, b , to the neighbouring bin, $b + 1$, would be less than the number of events migrating from bin, $b - 1$, to b . This effect is shown below in Figure 3.3.

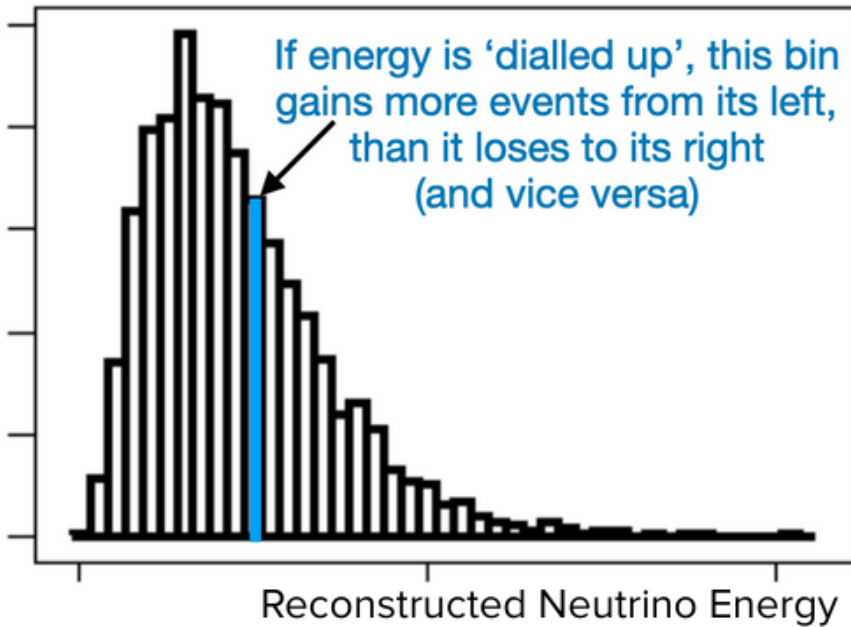


Figure 3.3.: Possible event migration due to uncertainty on the reconstructed neutrino energy.

Since the energy scale systematic is a global one, it is applied across all energy bins, for all modes, in the form a 1×1 covariance matrix.

3.5. Other Analysis Choices

All the stuff that was 'agreed' between fitters - Baseline Approximation, Binning, Spectra energy range etc.

3.5.1. Baseline

As is shown in Equation 1.33, the baseline is one of the components that drives the oscillation probability. For long baseline experiments, it's not uncommon for fitting frameworks to simply use some average value for the baseline since factors such as the interaction point in the detector or the position at which a particle decays into a neutrino would only change the average baseline for the experiment by a negligible amount.

However, for short baseline experiments such as SBN, these factors may change the baseline significantly.

In an attempt to minimise computing resources, the true baseline was not initially used, but instead, several approximations to the baseline were tried. To begin with, the average baseline of each SBN detector was used for all neutrino energies. This was calculated from the true baseline distribution of ν_μ events in each detector which are shown in Figure 3.4. Secondly, a 4-knot spline (named spline V1) for each detector was defined in order to try and better approximate the baseline. This method was improved upon by producing a spline for each of the true energy bins (named spline V2) which are defined in Section 3.5.2. In order to establish the impact of any baseline approximations on the oscillation probability, the oscillation probability was plotted as a function of true neutrino energy with the oscillation parameters $\sin^2 2\theta_{\mu\mu} = 0.01$ and $\Delta m_{41}^2 = 50 \text{ eV}^2$. This oscillation point was chosen to ensure that a region where rapid oscillations occur was being investigated, which would highlight the effect of any baseline choices. The oscillation probabilities as a function of energy are shown in Figure 3.6 for the four different baselines described. It was eventually decided that any approximation would be insufficient and that the true baseline should be used.

The studies of the baseline approximations were done in the context of the ν_μ disappearance channel. For the ν_e channels, different approximations should be applied, since the true baseline distribution is not the same as for ν_μ . In principle, within the ν_e sample, different approximations should be applied to the different sub-samples since the baseline distribution is not the same for all the sub-samples. This was never done since it was decided that the true baseline should be used. Each individual sample used to construct the overall ν_e event sample has its own baseline distribution due to the particles which contribute to each sample decaying at different points along the beamline. The baseline distribution for the intrinsic ν_e , oscillated ν_e and the overall ν_e sample from combining all the sub-samples together is shown in Figure 3.5 for each of the SBN detectors. It should be noted that the baseline distributions for oscillated ν_e sample from Figure 3.5 and the ν_μ sample from Figure 3.4 are comparable. This is due to the initial parameters describing the oscillated sample being the same as for the ν_μ sample. The only difference being the neutrino oscillations from ν_μ to ν_e which isn't something that affects the baseline.

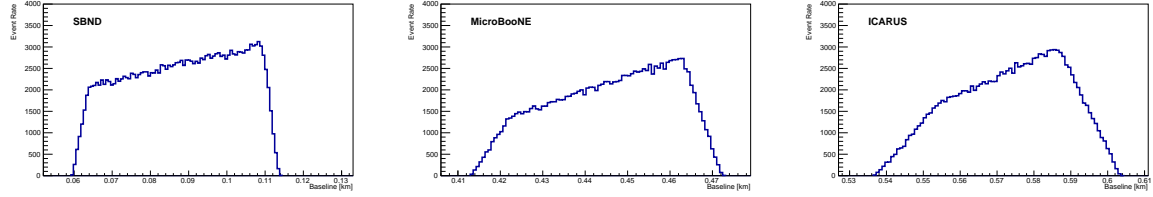


Figure 3.4.: The baseline distribution of events in the ν_μ sample for each of the SBN detectors.

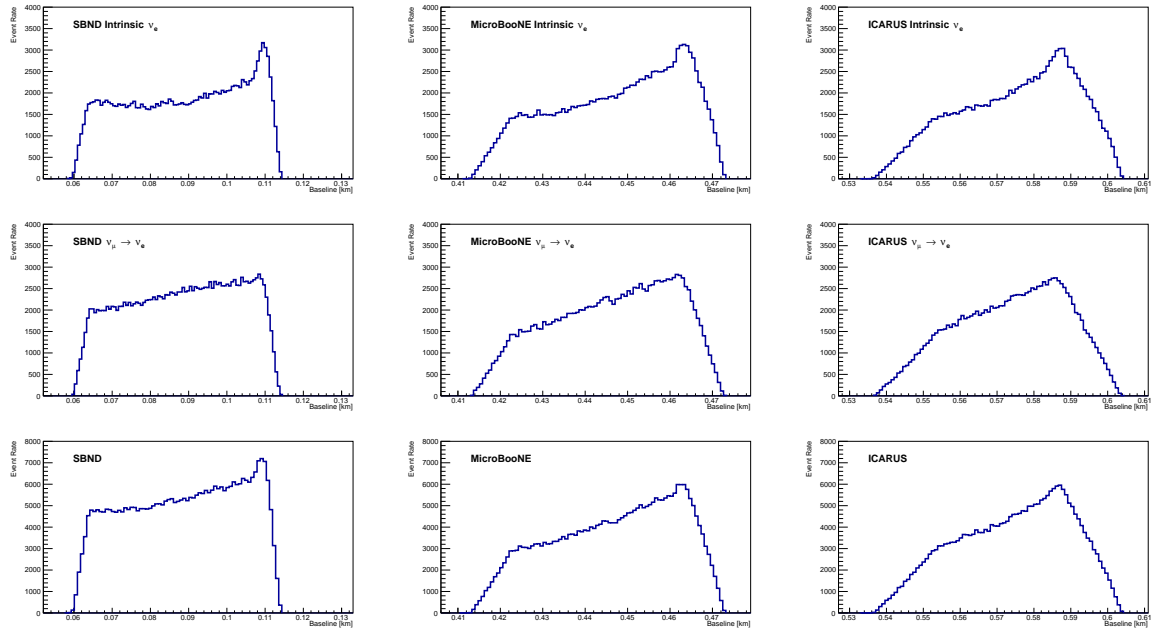


Figure 3.5.: The baseline distribution of events in each of the SBN detectors for the intrinsic ν_e sample (Top), the oscillated ν_e sample (Middle) and the overall ν_e sample (Bottom). The overall sample is comprised of the events from the intrinsic ν_e , oscillated ν_e , the ν_μ events from Figure 3.4 passing the ν_e selection and the dirt and cosmic samples (which are not explicitly shown).

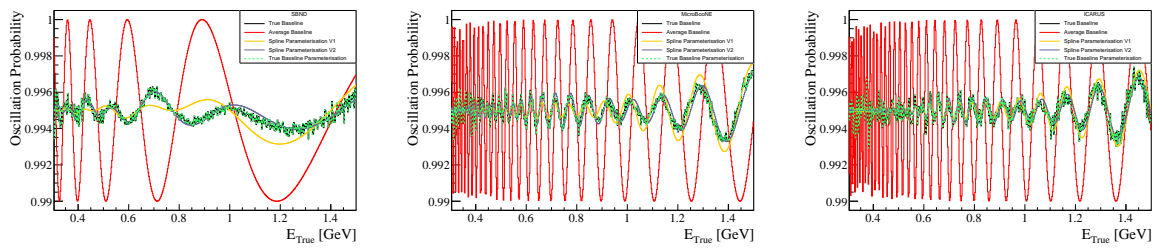


Figure 3.6.: The oscillation probability as a function of true neutrino energy for the ν_μ disappearance sample with oscillation parameters $\sin^2 2\theta_{\mu\mu} = 0.01$ and $\Delta m_{41}^2 = 50 \text{ eV}^2$ in each SBN detector. The results from using each baseline parametrisation are shown.

3.5.2. Binning

The energy binning schemes used to construct the Monte Carlo Templates (MCTs) are the same across each of the three detectors, however, the scheme used is different for the ν_μ and ν_e analyses. Furthermore, there are separate schemes for both the true and reconstructed energies. Each of the binning schemes is outlined below.

The ν_μ edge-to-edge binning has 21 bins in reconstructed neutrino energy which are bounded as follows:

- 1 bin from 0.00-0.20 GeV,
- 2 0.10-GeV bins from 0.20-0.40 GeV,
- 12 0.05-GeV bins from 0.40-1.00 GeV,
- 2 0.25-GeV bins from 1.00-1.50 GeV,
- 3 0.50-GeV bins from 1.50-3.00 GeV and
- 1 bin from 3.00-10.00 GeV.

The ν_μ edge-to-edge binning has 22 bins in true neutrino energy which are bounded as follows:

- 1 bin from 0.00-0.30 GeV,
- 3 0.10-GeV bins from 0.30-0.60 GeV,
- 12 0.05-GeV bins from 0.60-1.20 GeV,
- 1 bin from 1.20-1.50 GeV,
- 3 0.50-GeV bins from 1.50-3.00 GeV,
- 1 bin from 3.00-5.00 GeV and
- 1 bin from 5.00-10.00 GeV.

The ν_e edge-to-edge binning has 12 bins in reconstructed neutrino energy which are bounded as follows:

- 1 0.35-GeV bin from 0.00-0.35 GeV,
- 5 0.15-GeV bins from 0.35-1.10 GeV,
- 2 0.20-GeV bins from 1.10-1.50 GeV,
- 2 0.25-GeV bins from 1.50-2.00 GeV,
- 1 bin from 2.00-3.00 GeV and
- 1 bin from 3.00-10.00 GeV.

The ν_e edge-to-edge binning has 33 bins in true neutrino energy which are bounded as follows:

- 2 0.25-GeV bin from 0.00-0.50 GeV,
- 15 0.05-GeV bins from 0.50-1.25 GeV,
- 15 0.25-GeV bins from 1.25-5.00 GeV and
- 1 bin from 5.00-10.00 GeV.

Appendix A.

Pointless extras

Appendix B.

Single Parameter Variations

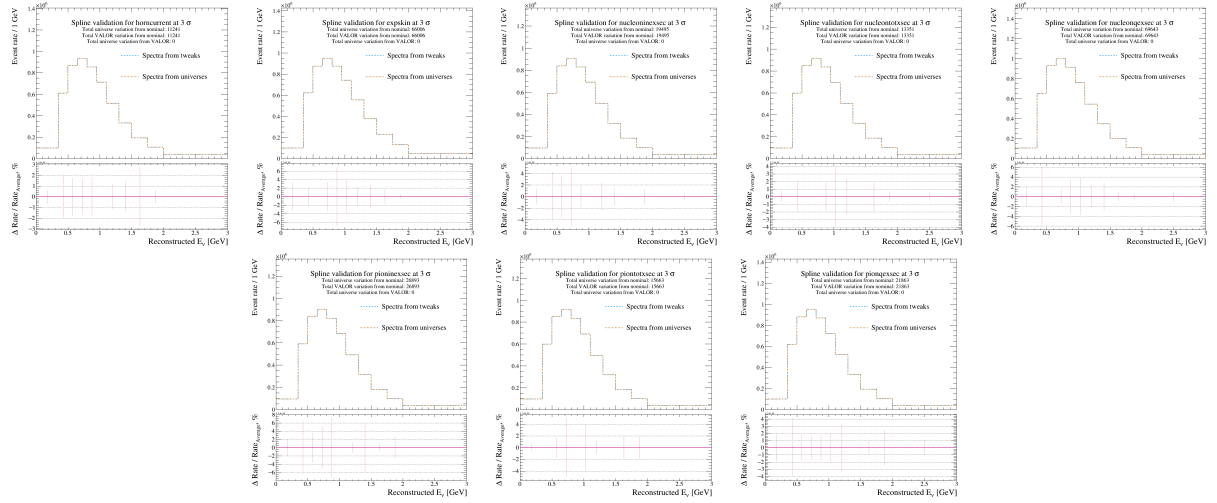


Figure B.1.: A comparison of the $+3\sigma$ variations from the response functions used by VALOR and the universes for the complete set of uncorrelated flux systematic parameters.

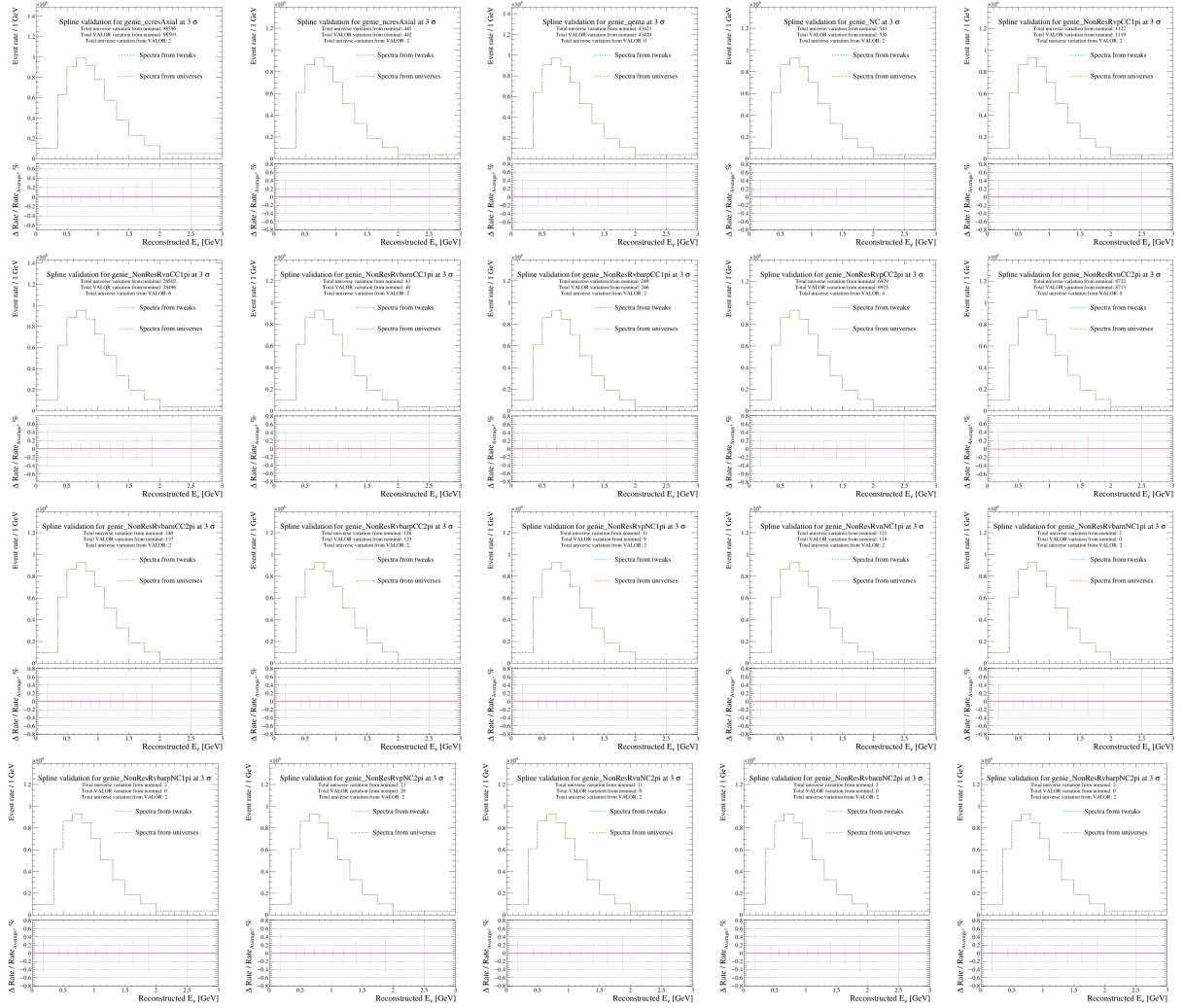


Figure B.2.: A comparison of the $+3\sigma$ variations from the response functions used by VALOR and the universes for the complete set of proposal interaction systematic parameters.

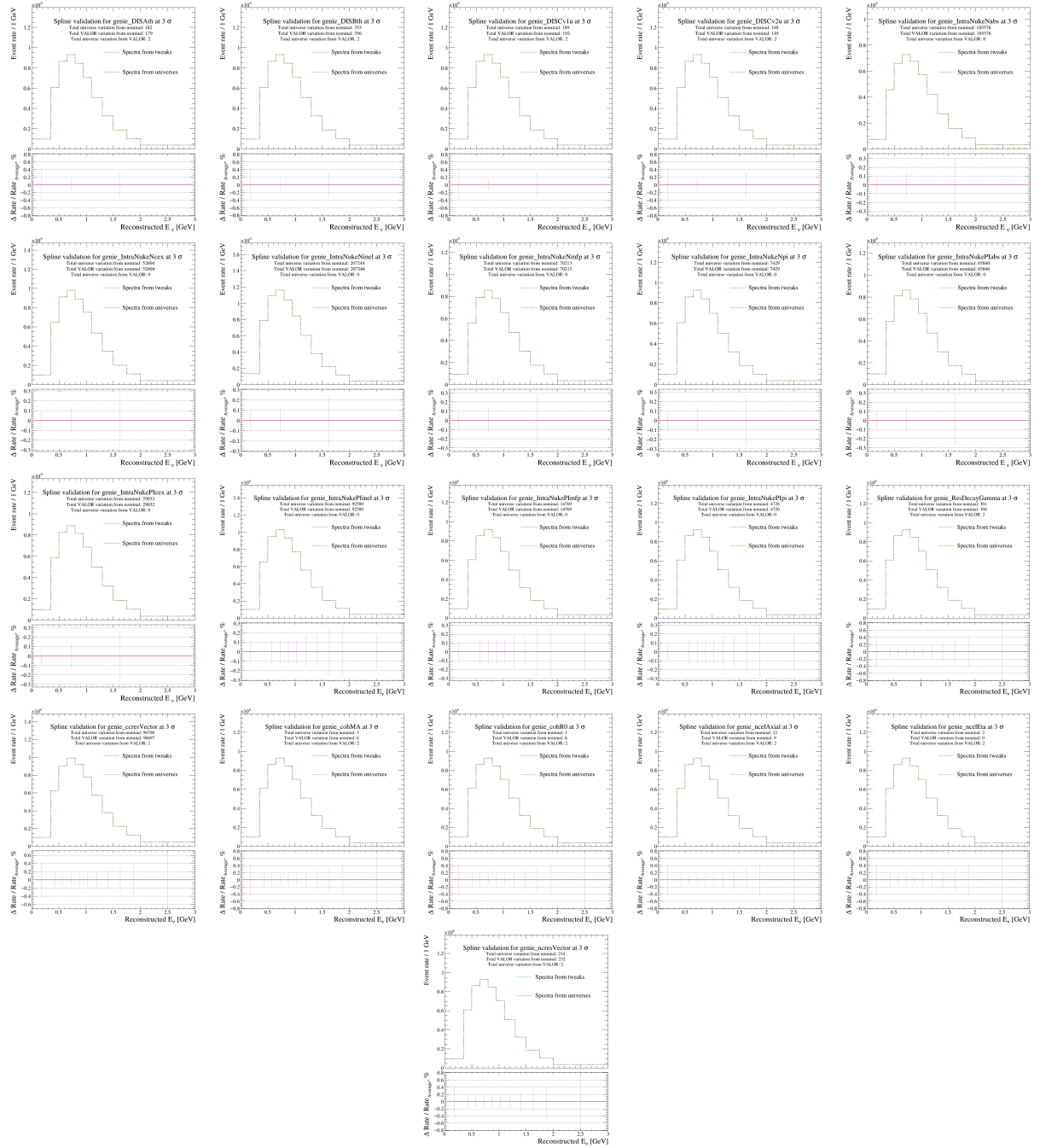


Figure B.3.: A comparison of the $+3\sigma$ variations from the response functions used by VALOR and the universes for the complete set of modern cross-section systematic parameters.

Colophon

This thesis was made in L^AT_EX 2 _{ε} using the “heptesis” class.

Bibliography

- [1] W. Pauli, Pauli letter collection: letter to Lise Meitner, <https://cds.cern.ch/record/83282>, Typed copy, [Accessed September 2021].
- [2] C. L. Cowan, Jr., F. Reines, F. B. Harrison, H. W. Kruse, and A. D. McGuire, Detection of the Free Neutrino: A Confirmation, [doi:10.1126/science.124.3212.103](https://doi.org/10.1126/science.124.3212.103), Science **124**, 103 (1956).
- [3] G. Danby *et al.*, Observation of High-Energy Neutrino Reactions and the Existence of Two Kinds of Neutrinos, [doi:10.1103/PhysRevLett.9.36](https://doi.org/10.1103/PhysRevLett.9.36), Physical Review Letters **9**, 36 (1962).
- [4] M. L. Perl *et al.*, Evidence for Anomalous Lepton Production in $e^+ - e^-$ Annihilation, [doi:10.1103/PhysRevLett.35.1489](https://doi.org/10.1103/PhysRevLett.35.1489), Phys. Rev. Lett. **35**, 1489 (1975).
- [5] DONUT, K. Kodama *et al.*, Observation of tau neutrino interactions, [doi:10.1016/S0370-2693\(01\)00307-0](https://doi.org/10.1016/S0370-2693(01)00307-0), Phys. Lett. **B504**, 218 (2001), hep-ex/0012035.
- [6] A. Blondel, The Number of Neutrinos and the Z Line Shape, [doi:10.1142/9789814733519_0008](https://doi.org/10.1142/9789814733519_0008), (2016).
- [7] ALEPH, D. Decamp *et al.*, Determination of the Number of Light Neutrino Species, [doi:10.1016/0370-2693\(89\)90704-1](https://doi.org/10.1016/0370-2693(89)90704-1), Phys. Lett. B **231**, 519 (1989).
- [8] LSND Collaboration, A. Aguilar *et al.*, Evidence for neutrino oscillations from the observation of $\bar{\nu}_e$ appearance in a $\bar{\nu}_\mu$ beam, [doi:10.1103/PhysRevD.64.112007](https://doi.org/10.1103/PhysRevD.64.112007), Phys. Rev. D **64**, 112007 (2001).
- [9] MiniBooNE Collaboration, A. A. Aguilar-Arevalo *et al.*, Significant Excess of Electron like Events in the MiniBooNE Short-Baseline Neutrino Experiment,

[doi:10.1103/PhysRevLett.121.221801](https://doi.org/10.1103/PhysRevLett.121.221801), Phys. Rev. Lett. **121**, 221801 (2018).

- [10] GALLEX, W. Hampel *et al.*, Final results of the Cr-51 neutrino source experiments in GALLEX, [doi:10.1016/S0370-2693\(97\)01562-1](https://doi.org/10.1016/S0370-2693(97)01562-1), Phys. Lett. B **420**, 114 (1998).
- [11] F. Kaether, W. Hampel, G. Heusser, J. Kiko, and T. Kirsten, Re-analysis of the Gallex solar neutrino flux and source experiments, [doi:<https://doi.org/10.1016/j.physletb.2010.01.030>](https://doi.org/10.1016/j.physletb.2010.01.030), Physics Letters B **685**, 47 (2010).
- [12] J. N. Abdurashitov *et al.*, Measurement of the response of a Ga solar neutrino experiment to neutrinos from a ^{37}Ar source, [doi:10.1103/PhysRevC.73.045805](https://doi.org/10.1103/PhysRevC.73.045805), Phys. Rev. C **73**, 045805 (2006).
- [13] G. Mention *et al.*, Reactor antineutrino anomaly, [doi:10.1103/physrevd.83.073006](https://doi.org/10.1103/physrevd.83.073006), Physical Review D **83** (2011).
- [14] S. Braibant, G. Giacomelli, and M. Spurio, *Particles and Fundamental Interactions: An Introduction to Particle Physics* Undergraduate Lecture Notes in Physics (Springer Netherlands, 2011).
- [15] E. Majorana, A Symmetric Theory of Electrons and Positrons, in *Scientific Papers of Ettore Majorana: A New Expanded Edition*, edited by L. Cifarelli, pp. 113–128, Springer International Publishing, Cham, 2020.
- [16] T. Morii , C. S. Lim , S. N. Mukherjee, *The Physics Of The Standard Model And Beyond* (World Scientific Publishing Co. Pte. Ltd., 2004).
- [17] W. H. Furry, On Transition Probabilities in Double Beta-Disintegration, [doi:10.1103/PhysRev.56.1184](https://doi.org/10.1103/PhysRev.56.1184), Phys. Rev. **56**, 1184 (1939).
- [18] V. Barger, D. Marfatia, and K. Whisnant, *The Physics of Neutrinos* (Princeton University Press, 2012).
- [19] B. R. Martin and G. Shaw, *Particle Physics, Third Edition* (John Wiley and Sons, Ltd, Publication, 2008).
- [20] M. Goldhaber, L. Grodzins, and A. W. Sunyar, Helicity of Neutrinos,

[doi:10.1103/PhysRev.109.1015](https://doi.org/10.1103/PhysRev.109.1015), Phys. Rev. **109**, 1015 (1958).

- [21] Alessandro De Angelis Mário Pimenta, *Introduction to Particle and Astroparticle Physics: Multimessenger Astronomy and its Particle Physics Foundations*, second ed. (Springer International Publishing AG, 2018).
- [22] C. Giunti and C. W. Kim, *Fundamentals of Neutrino Physics and Astrophysics*. (Oxford: Oxford University Press, 2007).
- [23] C. S. Wu, E. Ambler, R. W. Hayward, D. D. Hoppes, and R. P. Hudson, Experimental Test of Parity Conservation in Beta Decay, [doi:10.1103/PhysRev.105.1413](https://doi.org/10.1103/PhysRev.105.1413), Physical Review **105**, 1413 (1957).
- [24] J. H. Christenson, J. W. Cronin, V. L. Fitch, and R. Turlay, Evidence for the 2π Decay of the K_2^0 Meson, [doi:10.1103/PhysRevLett.13.138](https://doi.org/10.1103/PhysRevLett.13.138), Phys. Rev. Lett. **13**, 138 (1964).
- [25] A. D. Sakharov, Violation of CP invariance, C asymmetry, and baryon asymmetry of the universe, [doi:10.1070/pu1991v034n05abeh002497](https://doi.org/10.1070/pu1991v034n05abeh002497), Soviet Physics Uspekhi **34**, 392 (1991).
- [26] G. C. Branco, R. G. Felipe, and F. R. Joaquim, Leptonic CP Violation, [doi:10.1103/RevModPhys.84.515](https://doi.org/10.1103/RevModPhys.84.515), Rev. Mod. Phys. **84**, 515 (2012), 1111.5332.
- [27] F. Halzen and A. Martin, *Quarks and Leptons: An Introductory Course in Modern Particle Physics* (John Wiley, New York, 1984).
- [28] B. Pontecorvo, Neutrino Experiments and the Problem of Conservation of Leptonic Charge, Zh. Eksp. Teor. Fiz. **53**, 1717 (1967).
- [29] Z. Maki, M. Nakagawa, and S. Sakata, Remarks on the Unified Model of Elementary Particles, [doi:10.1143/PTP.28.870](https://doi.org/10.1143/PTP.28.870), Progress of Theoretical Physics **28**, 870 (1962), <https://academic.oup.com/ptp/article-pdf/28/5/870/5258750/28-5-870.pdf>.
- [30] K. Lande *et al.*, Results from the Homestake solar neutrino observatory, Conf. Proc. **C900802**, 867 (1990), [Conf. Proc.C900802V1,C900802V1:667(1990)].
- [31] Super-Kamiokande, J. G. Learned, The Atmospheric neutrino anomaly: Muon

neutrino disappearance, p. 89 (2000), hep-ex/0007056.

- [32] Y. Fukuda *et al.*, Evidence for Oscillation of Atmospheric Neutrinos, [doi:10.1103/physrevlett.81.1562](https://doi.org/10.1103/physrevlett.81.1562), Physical Review Letters **81**, 1562–1567 (1998).
- [33] SNO Collaboration, Q. R. Ahmad *et al.*, Measurement of the Rate of $\nu_e + d \rightarrow p + p + e^-$ Interactions Produced by 8B Solar Neutrinos at the Sudbury Neutrino Observatory, [doi:10.1103/PhysRevLett.87.071301](https://doi.org/10.1103/PhysRevLett.87.071301), Phys. Rev. Lett. **87**, 071301 (2001).
- [34] Particle Data Group, P. Zyla *et al.*, Review of Particle Physics, [doi:10.1093/ptep/ptaa104](https://doi.org/10.1093/ptep/ptaa104), PTEP **2020**, 083C01 (2020).
- [35] X. Qian and P. Vogel, Neutrino mass hierarchy, [doi:10.1016/j.ppnp.2015.05.002](https://doi.org/10.1016/j.ppnp.2015.05.002), Progress in Particle and Nuclear Physics **83**, 1–30 (2015).
- [36] R. N. Cahn *et al.*, White Paper: Measuring the Neutrino Mass Hierarchy, [doi:10.48550/ARXIV.1307.5487](https://doi.org/10.48550/ARXIV.1307.5487), 2013.
- [37] A. Diaz, C. Argüelles, G. Collin, J. Conrad, and M. Shaevitz, Where are we with light sterile neutrinos?, [doi:10.1016/j.physrep.2020.08.005](https://doi.org/10.1016/j.physrep.2020.08.005), Physics Reports **884**, 1 (2020).
- [38] KARMEN, K. Eitel, KARMEN: Present neutrino oscillation limits and perspectives after the upgrade, in *32nd Rencontres de Moriond: Electroweak Interactions and Unified Theories*, pp. 267–274, 1997, hep-ex/9706023.
- [39] MINOS Collaboration, P. Adamson *et al.*, Search for Sterile Neutrinos Mixing with Muon Neutrinos in MINOS, [doi:10.1103/PhysRevLett.117.151803](https://doi.org/10.1103/PhysRevLett.117.151803), Phys. Rev. Lett. **117**, 151803 (2016).
- [40] J. Kostensalo, J. Suhonen, C. Giunti, and P. Srivastava, The gallium anomaly revisited, [doi:<https://doi.org/10.1016/j.physletb.2019.06.057>](https://doi.org/10.1016/j.physletb.2019.06.057), Physics Letters B **795**, 542 (2019).
- [41] K. N. Abazajian *et al.*, Light Sterile Neutrinos: A White Paper, FERMILAB-PUB-12-881-PPD, [arXiv:1204.5379](https://arxiv.org/abs/1204.5379), 2012, 1204.5379.
- [42] P. A. Machado, O. Palamara, and D. W. Schmitz, The Short-Baseline Neutrino

Program at Fermilab, [doi:10.1146/annurev-nucl-101917-020949](https://doi.org/10.1146/annurev-nucl-101917-020949), Annual Review of Nuclear and Particle Science **69**, 363–387 (2019).

- [43] C. Rubbia, The Liquid Argon Time Projection Chamber: A New Concept for Neutrino Detectors, (1977).
- [44] R. Acciarri *et al.*, Design and Construction of the MicroBooNE Detector, [doi:10.1088/1748-0221/12/02/P02017](https://doi.org/10.1088/1748-0221/12/02/P02017), Journal of Instrumentation **12** (2016).
- [45] M. Schenk, *Studies with a Liquid Argon Time Projection Chamber: Addressing Technological Challenges of Large-Scale Detectors* BestMaster, 1 ed. (Springer Specktrum, 2015).
- [46] Y. Li *et al.*, Measurement of longitudinal electron diffusion in liquid argon, [doi:10.1016/j.nima.2016.01.094](https://doi.org/10.1016/j.nima.2016.01.094), Nuclear Instruments and Methods in Physics Research Section A: Accelerators, Spectrometers, Detectors and Associated Equipment **816**, 160–170 (2016).
- [47] C. Anderson *et al.*, The ArgoNeuT detector in the NuMI low-energy beam line at Fermilab, [doi:10.1088/1748-0221/7/10/p10019](https://doi.org/10.1088/1748-0221/7/10/p10019), Journal of Instrumentation **7**, P10019–P10019 (2012).
- [48] G. Jaffé, Zur Theorie der Ionisation in Kolonnen, [doi:<https://doi.org/10.1002/andp.19133471205>](https://doi.org/10.1002/andp.19133471205), Annalen der Physik **347**, 303 (1913), <https://onlinelibrary.wiley.com/doi/pdf/10.1002/andp.19133471205>.
- [49] J. Thomas and D. A. Imel, Recombination of electron-ion pairs in liquid argon and liquid xenon, [doi:10.1103/PhysRevA.36.614](https://doi.org/10.1103/PhysRevA.36.614), Phys. Rev. A **36**, 614 (1987).
- [50] M. Mooney, The MicroBooNE Experiment and the Impact of Space Charge Effects, [doi:10.48550/ARXIV.1511.01563](https://arxiv.org/abs/1511.01563), 2015.
- [51] S. Palestini and K. McDonald, Space charge in ionization detectors, <https://physics.princeton.edu/examples/spacecharge.pdf>, 2016, [Accessed: August, 2022].
- [52] V. Shiltsev, Fermilab Proton Accelerator Complex Status and Improvement Plans, [doi:10.1142/S0217732317300129](https://doi.org/10.1142/S0217732317300129), Mod. Phys. Lett. A **32**, 1730012 (2017), 1705.03075.

- [53] SciBooNE, A. A. Aguilar-Arevalo *et al.*, Bringing the SciBar detector to the booster neutrino beam, (2006), hep-ex/0601022.
- [54] MiniBooNE Collaboration, A. A. Aguilar-Arevalo *et al.*, Neutrino flux prediction at MiniBooNE, [doi:10.1103/PhysRevD.79.072002](https://doi.org/10.1103/PhysRevD.79.072002), Phys. Rev. D **79**, 072002 (2009).
- [55] LAr1-ND, ICARUS-WA104, MicroBooNE, M. Antonello *et al.*, A Proposal for a Three Detector Short-Baseline Neutrino Oscillation Program in the Fermilab Booster Neutrino Beam, [arXiv:1503.01520](https://arxiv.org/abs/1503.01520), 2015, 1503.01520.
- [56] C. E. Patrick, *Measurement of the Antineutrino Double-Differential Charged-Current Quasi-Elastic Scattering Cross Section at MINERvA* (Springer International Publishing, Cham, 2018).
- [57] E. Scantamburlo, *Measurement of the Water to Scintillator Charged-Current Cross-Section Ratio for Muon Neutrinos at the T2K Near Detector*, PhD thesis, UNIVERSITÉ DE GENÈVE, 2017, Presented 06 Jun 2017.
- [58] M. Acero *et al.*, Adjusting neutrino interaction models and evaluating uncertainties using NOvA near detector data, [doi:10.1140/epjc/s10052-020-08577-5](https://doi.org/10.1140/epjc/s10052-020-08577-5), The European Physical Journal C **80** (2020).
- [59] T. Van Cuyck, N. Jachowicz, R. González-Jiménez, J. Ryckebusch, and N. Van Dessel, Seagull and pion-in-flight currents in neutrino-induced $1n$ and $2n$ knockout, [doi:10.1103/PhysRevC.95.054611](https://doi.org/10.1103/PhysRevC.95.054611), Phys. Rev. C **95**, 054611 (2017).
- [60] K. Majumdar and K. Mavrokoridis, Review of Liquid Argon Detector Technologies in the Neutrino Sector, [doi:10.3390/app11062455](https://doi.org/10.3390/app11062455), Applied Sciences **11**, 2455 (2021).
- [61] M. Auger *et al.*, A novel cosmic ray tagger system for liquid argon tpc neutrino detectors, [doi:10.48550/ARXIV.1612.04614](https://doi.org/10.48550/ARXIV.1612.04614), 2016.
- [62] C. Adams *et al.*, Design and construction of the MicroBooNE Cosmic Ray Tagger system, [doi:10.1088/1748-0221/14/04/p04004](https://doi.org/10.1088/1748-0221/14/04/p04004), Journal of Instrumentation **14**, P04004–P04004 (2019).
- [63] A. Machado and E. Segreto, ARAPUCA a new device for liquid argon scintillation light detection, [doi:10.1088/1748-0221/11/02/c02004](https://doi.org/10.1088/1748-0221/11/02/c02004), Journal of Instrumentation **11**,

C02004 (2016).

- [64] A. Machado *et al.*, The X-ARAPUCA: an improvement of the ARAPUCA device, [doi:10.1088/1748-0221/13/04/c04026](https://doi.org/10.1088/1748-0221/13/04/c04026), Journal of Instrumentation **13**, C04026–C04026 (2018).
- [65] R. Acciarri *et al.*, Design and construction of the MicroBooNE detector, [doi:10.1088/1748-0221/12/02/p02017](https://doi.org/10.1088/1748-0221/12/02/p02017), Journal of Instrumentation **12**, P02017–P02017 (2017).
- [66] Sandbox Studio, Chicago, Schematic of the ICARUS detector., <https://www.symmetrymagazine.org/article/sterile-neutrino-sleuths>, [Accessed: January, 2022].
- [67] ICARUS Collaboration, C. Rubbia and C. S. Montanari, Status and plans of WA104/ICARUS, CERN-SPSC-2017-012, SPSC-SR-207, <https://cds.cern.ch/record/2256748>, 2017.
- [68] C. Frugueule, Probing sub-GeV dark sectors via high energy proton beams at LBNF/DUNE and MiniBooNE, [doi:10.1103/PhysRevD.96.015029](https://doi.org/10.1103/PhysRevD.96.015029), Phys. Rev. D **96**, 015029 (2017).
- [69] P. Ballett, S. Pascoli, and M. Ross-Lonergan, MeV-scale sterile neutrino decays at the Fermilab Short-Baseline Neutrino program, [doi:10.1007/jhep04\(2017\)102](https://doi.org/10.1007/jhep04(2017)102), Journal of High Energy Physics **2017** (2017).
- [70] E. Bertuzzo, S. Jana, P. A. N. Machado, and R. Zukanovich Funchal, Dark Neutrino Portal to Explain MiniBooNE Excess, [doi:10.1103/PhysRevLett.121.241801](https://doi.org/10.1103/PhysRevLett.121.241801), Phys. Rev. Lett. **121**, 241801 (2018).
- [71] C. Andreopoulos *et al.*, The GENIE Neutrino Monte Carlo Generator, [doi:10.1016/j.nima.2009.12.009](https://doi.org/10.1016/j.nima.2009.12.009), Nucl. Instrum. Meth. A **614**, 87 (2010), 0905.2517.
- [72] GEANT4 A Simulation Toolkit, <https://geant4.web.cern.ch/>, [Accessed August, 2022].
- [73] LArSoft, <https://larsoft.org/>, [Accessed: July, 2022].

- [74] D. Schmitz, SBND POT and Event Estimates, <https://sbn-docdb.fnal.gov/cgi-bin/sso>ShowDocument?docid=27405>, 2022, [Accessed: Aug, 2022].
- [75] R. Jones, *Muon-neutrino disappearance with multiple liquid argon time projection chambers in the Fermilab Booster neutrino beam*, PhD thesis, doi:10.17638/03143192, University of Liverpool, 2021.
- [76] D. Barker, *Developments Towards a ν_e CC Sterile Appearance Sensitivity in the Short-Baseline Neutrino Programme*, PhD thesis, uk.bl.ethos.832514, University of Sheffield, 2020.
- [77] C. Andreopoulos *et al.*, The GENIE Neutrino Monte Carlo Generator: Physics and User Manual, 2015, 1510.05494.
- [78] MicroBooNE Collaboration, Booster Neutrino Flux Prediction at MicroBooNE, doi:10.2172/1573216, (2018).